PHYSICA

STUDIA
UNIVERSITATIS BABEŞ-BOLYAI
PHYSICA

1-2/2019
January-December

S T U D I A
UNIVERSITATIS BABEŞ–BOLYAI

PHYSICA

1-2

CUPRINS – CONTENT – SOMMAIRE – INHALT

CALCULATIONS ON e$^+$ - N$_2$ IONIZATION

R. I. CAMPEANU[1], I. TÓTH[2*] and L. NAGY[2]

ABSTRACT. Positron impact direct ionization cross sections are calculated for molecular nitrogen using two distorted wave models. The results are compared with the latest experimental and theoretical data available.

Keywords: ionization, positron, nitrogen molecule

INTRODUCTION

Positron collision phenomena with molecular targets have attracted much interest in the last decades. Potential improvements in applications like positron emission tomography provide an additional motivation for studying such collision phenomena. Experimental measurements for the ionization of several molecules by positrons have been carried out over the years. These molecules include simple ones like H_2 [1, 2], N_2 [3–5], O_2 [5, 6] or more complex ones like CO [5, 7], CH_4 [7] and CO_2 [7, 8]. For N_2 even differential studies are available [9].

On the theory side we studied the positron impact ionization of several molecules using distorted wave methods and a Gaussian-type multicenter molecular wavefunction [10,11]. We obtained a particularly good agreement with the experimental data for N_2 of ref. [3]. In another study [12] the Spherical Complex Optical Potential (SCOP) method was employed to calculate ionization cross section for several molecules, including N_2. These calculations also showed a good agreement with the experimental data [3].

Our present study is motivated by the publication of a new set of experimental data [4], which showed smaller cross section values than those measured in [3]. We introduce two models in order to calculate the direct ionization cross section

---

[1] *York University, Department of Physics and Astronomy, 4700 Keele Street, Toronto, Canada M3J 1P3*

[2] *Babeş-Bolyai University, Faculty of Physics, 1 Kogălniceanu str., 400084 Cluj-Napoca, Romania*

* Corresponding author: istvan.toth@phys.ubbcluj.ro

for N_2 in collision with positron projectiles and compare the new results with the existent experimental and theoretical data.

THEORY

The ionization cross section of a molecular target can be calculated by integrating the triple-differential cross section

$$\frac{d^3\sigma}{d\mathbf{k}_f d\mathbf{k}_e dE_e} = \sum_n \frac{(2\pi)^4}{E_i} |f^n|^2 \tag{1}$$

which is a function of several physical quantities, like the projectile energy E_i, the energy of the ejected electron E_e and the scattering angles of the momenta of the outgoing particles. The sum in the above equation is performed over all occupied molecular orbitals. The scattering amplitude, f^n may be written as

$$f^n = \langle \phi_f(\mathbf{r_1})\phi_e(\mathbf{r_2})|V(r_{12})|\phi_i(\mathbf{r_1})\phi_b^n(\mathbf{r_2})\rangle \tag{2}$$

In equation (2), ϕ_i, ϕ_e and ϕ_f stand for the wavefunctions of the incident, ejected and scattered particles, while ϕ_b^n describes the bound state of the active electron represented as a Gaussian-type multicenter wavefunction [10]. The position vector of the active electron is $\mathbf{r_2}$, while $\mathbf{r_1}$ is the corresponding vector for the projectile. $V(r_{12})$ is the interaction potential between the projectile and the active electron. In order to separate the radial and angular part of the multicenter bound state, we expand it in terms of the Legendre polynomials for σ orbitals:

$$\phi_b^n(\mathbf{r_2}) = \sum_{l_b} y_{l_b}^n(r_2, R) P_{l_b}(\cos \omega_2) \tag{3}$$

where the expansion coefficient can be calculated as

$$y_{l_b}^n(r_2, R) = \frac{2l_b+1}{2} \int_{-1}^{1} d(\cos \omega_2) P_{l_b}(\cos \omega_2) \phi_b^n(\mathbf{r_2}) \tag{4}$$

Here, l_b stands for the orbital angular momentum quantum number of the bound state electron and R is the internuclear separation, while ω_2 is the angle between $\mathbf{R}$ and $\mathbf{r_2}$. The expansion cannot be applied directly to $\boldsymbol{\pi}$ orbitals due to the dependence on the $\boldsymbol{\varphi}$ angle of such states, hence a transformation to the centre of mass coordinates is applied before the expansion. Further, we apply a transformation

from the molecular frame to the laboratory frame. These transformations are all detailed in [10]. The wavefunctions of the free particles were expanded into partial wave series. Performing all these calculations the triple-differential cross section may be written as a sum of cross sections characterized by a certain angular momentum of the initial state with quantum numbers l_b and m_b:

$$\frac{d^3\sigma}{dk_f dk_e dE_e} = \sum_n \sum_{l_b m_b} \frac{(2\pi)^4}{E_i} \left| f_{l_b m_b}^n \right|^2 \qquad (5)$$

where $f_{l_b m_b}^n$ is the partial scattering amplitude for orbital n. In the laboratory frame the molecule can have an arbitrary orientation, therefore we must average the cross section (5) over all possible orientations of $\boldsymbol{R}$. In order to obtain the total ionization cross section the differential cross section is integrated over the angles of the outgoing particles and the energy of the ejected electron.

In order to calculate the ionization cross section, we use two different approaches to the wavefunctions of the particles involved in the process. The first model, employs Coulomb waves for describing the outgoing particles, while the incoming projectile is described by a plane wave. This can be formalized in terms of the potentials 'seen' by the particles as follows:

$$\begin{cases} V_i = 0 \\ V_e = -\frac{1}{r} \\ V_f = \frac{1}{r} \end{cases} \qquad (6)$$

Here, V_i, V_e and V_f are the potential energies for the incoming, ejected and scattered particles. We call the above ensamble of potentials the CCA (Coulomb-Coulomb Approximation) model, which refers to the Coulomb wave functions describing the outgoing particles, calculated by solving the radial Schrödinger equation for these potentials. The CCA model was first introduced for the description of the positron impact ionization of the helium atom [13]. In a second model, called TSS (Total Screening - Symmetric) we have calculated the wave functions of the free particles by employing the potentials detailed below:

$$\begin{cases} V_i = V_{nuclei} - V_{electrons} \\ V_e = -V_{nuclei} - V_{electrons}^- \\ V_f = V_{nuclei} - V_{electrons}^- \end{cases} \qquad (7)$$

where V_{nuclei} , $V_{electrons}$ and $V_{electrons}^-$ are the spherically averaged potentials of the nuclei, electrons and residual electrons, respectively. These potentials provided distorted waves for the description of the continuum states by solving the radial Schrödinger equation. The averaging of these potentials was detailed in [11].

RESULTS

Figure 1 shows our CCA and TSS results compared with two of the existing experimental sets of data and with our previous theoretical cross sections and the theoretical calculations of [12]. The data of Bluhme et al [3] were obtained by normalizing the relative experimental cross sections to the theoretical cross sections of Krishnakumar et al [14], while the data of Cooke et al [4] were obtained by normalizing their relative cross sections to the electron impact cross sections measured with the same apparatus. We also show in Figure 1 the experimental data of Marler and Surko [5], which include contributions from dissociative ionization too, hence the large disagreement with the Cooke et al [4] experiment. Our models CPE, ES and TS were employed to calculate positron impact ionization cross sections for several molecules including N_2 [11]. All these models take into account the screening of the residual ion by the slower particle. If the scattered projectile is faster than the ejected electron, the model assumes that the ejected electron moves in the spherically averaged potential field of the nuclei and residual electrons, while the projectile is essentially described by a plane wave. For an ejected electron faster than the scattered positron, the electron moves in the averaged field of the nuclei-positron and the averaged field of the residual electrons, while the positron is described by a Coulomb wave. The difference between the 3 models is in the way they include the screening. ES (Electron Screening) considers the screening only for the ejected electron, TS (Total Screening) considers screening for all free particles, while CPE uses only Coulomb and plane waves. Figure 1 shows that the our ES and the SCOP calculations of [12] are in very good agreement with the experimental data of Bluhme et al [3]. In the CCA and TSS models both outgoing particles move in the field of the residual ion independent of their energies. In the CCA model the wavefunctions of the outgoing particles are Coulomb waves calculated by employing the potential of the residual ion, while in the TSS model both outgoing particles move in the spherically averaged potential of the nuclei and residual electrons. In ref. [13] model CCA was shown to produce ionization cross sections significantly lower than the CPE model. The same is seen in Figure 1. Both the CCA and TSS model provide cross sections which are lower than those of the CPE, ES and TS models. The height of the peak in the CCA and TSS curves is similar to the height of the peak in the experimental data of Cooke et al [4], but the theoretical peaks appear at an impact energy of 200 eV, while the experimental peak at 80-100 eV. This shift is probably the consequence of the simplification we employed in our models, that both particles move in the field of the residual ion, regardless of their energy.
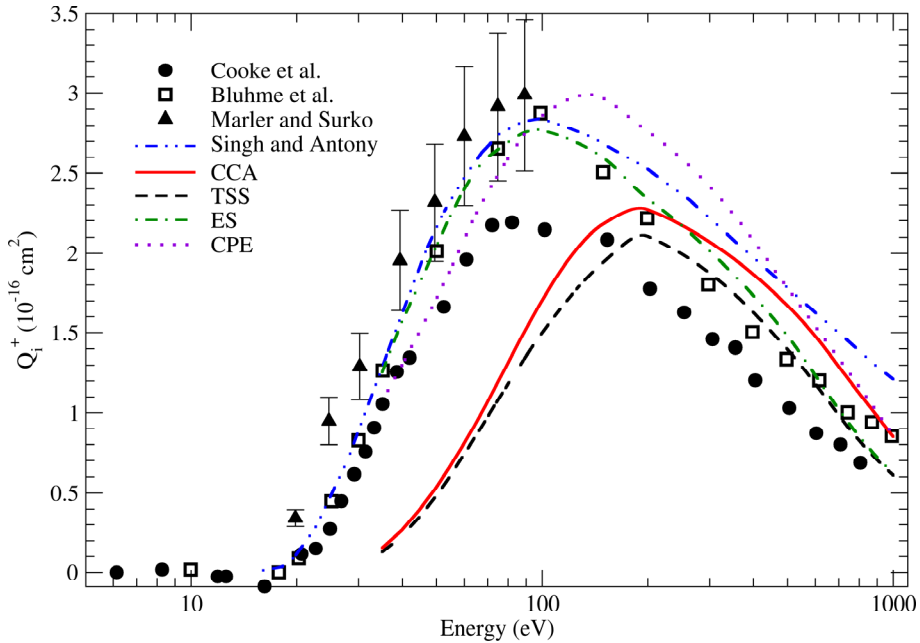
Fig. 1. Direct ionization cross sections for the N$_2$ molecule as a function of the impact energy of the positron. Our present results are provided by the CCA and TSS models, compared with the experimental data of [3] and [4] and the theoretical calculations of [12]. Our previously calculated results are also shown for the CPE, ES and TS models [11].

CONCLUSIONS

We have calculated direct ionization cross sections for the ionization of N$_2$ by positron projectiles using two distorted wave models and we compared them with the existent experimental data and theoretical calculations. This work was motivated by the discrepancy between the experimental cross sections of Cooke et al [4] and Bluhme et al [3]. Our current theoretical results, obtained by employing the CCA and TSS models, showed similar values for the ionization cross section as the data of Cooke et al [4], but the theoretical peaks were shifted relative to the experimental peak to higher impact energies. The best agreement between theory and experiment was obtained in the case of model ES and the experimental data of Bluhme et al [3].

ACKNOWLEDGEMENTS

REFERENCES

1. J. Moxom, P. Ashley, G. Laricchia, *Can. J. Phys*., 74, 367 (1996)
2. F.M. Jacobsen, N.P. Frandsen, H. Knudsen, U. Mikkelsen, *J. Phys. B: At. Mol. Opt. Phys.,* 28, 4675 (1995)
3. H. Bluhme, N.P. Frandsen, F.M. Jacobsen, H. Knudsen, J. Merrison, K. Paludan, M.R. Poulsen, *J. Phys. B: At. Mol. Opt. Phys.,* 31, 4631 (1998)
4. D. A. Cooke, D J. Murtagh and G. Laricchia, *Eur. Phys. J. D,* 68, 66 (2014)
5. J. P. Marler and C. M. Surko, *Phys. Rev. A*, 72, 062713 (2005)
6. G. Laricchia, J. Moxom, M. Charlton, *Phys. Rev. Lett.*, 70, 3229 (1993)
7. H. Bluhme, N.P. Frandsen, F.M. Jacobsen, H. Knudsen, J. Merrison, R. Mitchell, K. Paludan, M.R. Poulsen, *J. Phys. B: At. Mol. Opt. Phys.,* 32, 5825, (1999)
8. G. Laricchia, J. Moxom, *Phys. Lett. A*, 174, 255, (1993)
9. O. G. de Lucio and R. D. DuBois, *Phys. Rev. A,* 93, 032710, (2016)
10. R. I. Campeanu, V. Chis, L. Nagy and A. D. Stauffer, *Nucl. Instrum. Meth. B,* 221, 21 (2004)
11. I. Toth, R. I. Campeanu, V. Chis, L. Nagy, *Phys. Lett. A,* 360, 131 (2006)
12. S. Singh and B. Antony, EPL 119, 50006 (2017)
13. R. I. Campeanu, R. P. McEachran and A. D. Stauffer, *J. Phys. B: At. Mol. Phys.*, 20, 1635 (1987)
14. E. Krishnakumar and S. K. Srivastava, *J. Phys. B: At. Mol. Phys.*, 23, 1893 (1990)

HOW SHORT IS A SEMI-INFINITE LADDER? AN EXPERIMENTAL APPROACH

L. CSILLAG[1], A. TUNYAGI[1], ZS. LÁZÁR[1] and A. SIMON[1*]

ABSTRACT. This paper presents the challenging problem of solving of a semi-infinite resistive ladder and highlights some traps and tricks of the subject. The topic is approached from and experimental point of view by solving it using computation, simulation and measurements. All the work was done with the hope that it can be an aid for Physics or Electrical Engineering teachers, students eager to learn and understand more, and to be usefully incorporated into the educational process of talented pupils and students.

Keywords: semi-infinite resistive ladder, equivalent resistance, experimental approach, analytical solution

INTRODUCTION

Electrical circuits and networks are important components of high-school, college and university teaching curricula. At high-school level, the teaching process is based only on Ohm's and Kirchhoff's laws with simple calculus, but later, at undergraduate level, this knowledge is being completed by several new laws and network theorems (Thevenin, Norton, Millman, etc.) and some advanced Mathematics.

At introductory levels of teaching it is customary to illustrate the above-mentioned laws and theorems with the general problem of calculating the equivalent resistance (or impedance) of some, good looking, not very complicated series, parallel or mixed arrangements and combinations of elements. More complicated arrangements (cube, hexagon, flower, ladder, square grid, toroid, polyhedron, fractals, etc.) of a larger number of elements, or even an infinity of them, have several solving

[1] *Babeș-Bolyai University, Faculty of Physics, 1 M. Kogălniceanu street, 400084 Cluj-Napoca, Romania*
* *Corresponding author: alpar.simon@phys.ubbcluj.ro*

traps or tricks, but leading towards some elegant solutions [1-21]. Moreover, the experimental approach to this problem is rather neglected in the scientific literature [4, 5, 22, 23].

Including infinity in those networks, at least at the first sight, tends to complicate the solving of the problem, and making that type of problem being an excellent example and support of the general idea that only classical, fundamental knowledge is not sufficient to cope with such problems, open mindedness and both flexibility and creativity in thinking is necessary.

The problem of infinite resistance (or equivalent) is a very interesting and challenging topic from both scientific and pedagogic point of view. The scientific or practical applications may include transmission lines and networks, filters, digital to analog conversion, geophysical prospection, automatized error testing etc. The theoretical and pedagogical aspects are dealing with some important topics of Physics, Mathematics or Electrical Engineering teaching such as random walk, discrete variable Fourier transforms, lattice Green's function, golden ratio, Fibonacci sequence, computer-based simulation and programming, etc.

University students could land in difficulty when try to solve an infinite network. In fact, this later ascertainment, made on own students, was the starting point of this paper: a short (15 minute) test was given to 2nd year Physics students at the end of a complete, one semester long Electricity and Magnetism Course, the task was to find the equivalent resistance of an infinite resistive ladder. The results of the test are supporting the general idea that only classical, fundamental knowledge is not sufficient to cope with such problems, open mindedness and both flexibility and creativity in thinking is necessary: 14.8 % of the students approached the problem via network theorems, but getting into an impasse after analyzing the first two loops, 40.7 % of them approached the problem via mathematical induction, from one unit towards the nth one, but getting into a dead end after analyzing just two loops, 26 % have written the expressions of series and parallel resistances completely wrong after the first loop, finding out no solution for the network and finally 18.5 % of them solved the problem correctly, but all of them were former participants to Physics problem solving contest during high-school.

As we stated before, the study of infinite networks goes beyond fundamental knowledge, requiring creative and flexible thinking. This paper is trying to deal with the teaching challenges of a semi-infinite resistive ladder and approaching to it from both analytical and experimental point of views. We have tried to solve it using computation, simulation and measurements, in all cases highlighting the traps and tricks of the subject, emphasizing on how the analytical and experimental approaches, together with simulation sustain and complete each other. All the work was done with the hope that it can be usefully incorporated into the educational process of talented pupils and students.

THE ANALYTICAL APPROACH TO THE RESISTIVE LADDER
A. THE GENERAL CASE ($R_1 \neq R_2$)

The ladder circuit, or attenuation chain, is a simpler particular case of the two-dimensional infinite network of resistors. It is semi-infinite because it has a pair of starting connection point (A and B) and extends towards infinity only in one direction. It is built by successive adding of units of loops of series connected resistors R_1 and R_2, the next unit being always connected in parallel with resistor R_2 from the previous unit (Fig. 1). The eternal question is to find the equivalent resistance $R_{eq}^{(n)}$ of such a ladder [24, 25]
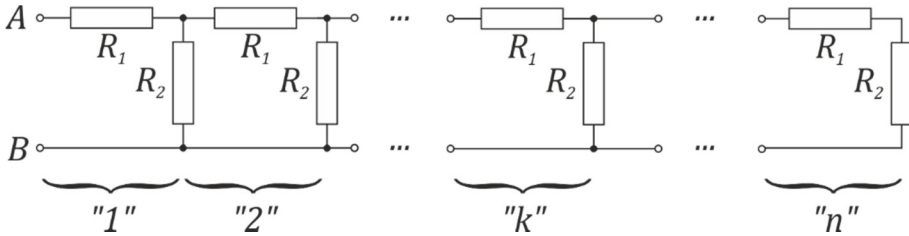
Fig. 1 Semi-infinite resistive ladder

Usually, the problems involving infinity may intimidate solvers and classical approaches may not work, but in the same time, such a problem will be very useful as an educational tool towards developing a scientific open mindedness, flexibility and creativity in thinking.

Finding out the equivalent resistance of such an infinite circuit is a well-known classical problem, with an elegant solution and several, both theoretical or experimental solving approaches, but the nodal voltages, branch currents, attenuation for the same type of network are less more discussed in the literature.

In spite of the infinite number of resistors the series connected resistors tend to increase, the parallel connected ones tend to decrease the equivalent resistance. Therefore, the expected equivalent resistance will not be infinite due to the mutual compensation of the effects induced by both R_1 and R_2, and the nodal voltages and branch currents are expected to be almost zero at far end of the ladder.

In the case of infinities, the solver is tempted to try mathematical induction: start with two repeating blocks, calculate the equivalent resistance, then increase the number of blocks by one, calculate again, and so on … until some recursive formula is found, but it is a hard work with persistence and extra attention being crucial during deduction. And the result is not very foreseeable.

As it was also highlighted by Kagan and Wang [26], here comes the first trap of the solving: when increasing the number of repeating blocks, the new pair of R_1 and R_2 could be added to the left or to the right from the existing circuit. Adding to the right has an experimental, circuit building technique type of logic, and contrarily, the adding to the left has apparently no justification, being the only alternative to the right side of the ladder. This latter approach may be supported also by the logical thinking that suggests to extend the finite end of the ladder (from points A and B to the left, Fig.1) and not the far-right end, already being at infinity.

Anyway, the trick of solving a semi-infinite ladder is simple and elegant, having nothing related to Physics or Electrical Engineering, but only to logical thinking: if the ladder is semi-infinite, already containing an infinity of resistor pairs, its equivalent resistance is not depending on the number of pair units (n) and will not be changed by adding one more unit (or even cutting down one, if the ladder already existed):

$$R_{eq}^{(n+1)} = R_{eq}^{(n)} = R_{eq}^{(n-1)} = R_{eq}^{(\infty)} \tag{1}$$

How to get out from the trap of the "ladder end"? Kagan and Wang [26] suggest that adding one more unit to the right of the existing circuit would violate the assumption that in the rightmost unit R_1 and R_2 are in series. This assumption needs some correcting amendments: (i) by adding the new pair of R_1 and R_2 to the right of the ladder already containing n units, we increase this number to $n + 1$, and face a parallel connection between the the nth R_2 and the new unit (R_1, R_2), but in the new last unit (the $n + 1^{\text{th}}$ one) R_1 and R_2 will still be in series (see Fig.2), (ii) when adding a new unit from the right of the ladder, the connection is not made between reference points A and B, representing the desired equivalent resistance given by Eq.1, but between points B and C (see Fig. 2) and the presumption of not changing the equivalent resistance $R_{eq}^{(\infty)}$ will not stand anymore!
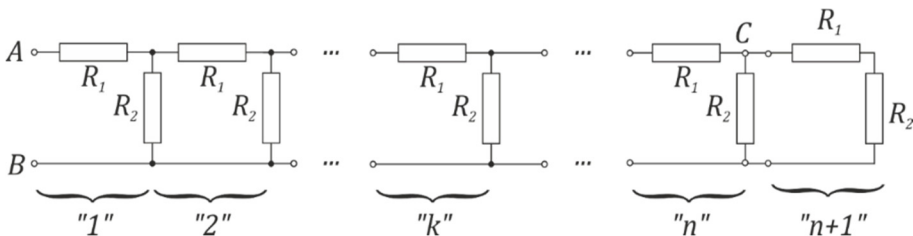
Fig. 2 Adding an extra unit to the right of the ladder

Let's analyze now the finite end of the ladder. By adding the new pair of R_1 and R_2 to the left of the ladder already containing n units we will also increase this number to $n + 1$, and have to deal with a parallel connection between R_2 and the initial ladder, all being in series connection to R_1. Thus, the equivalent resistance in this case will be (see Fig. 3, Eq.1 and Eq.2):
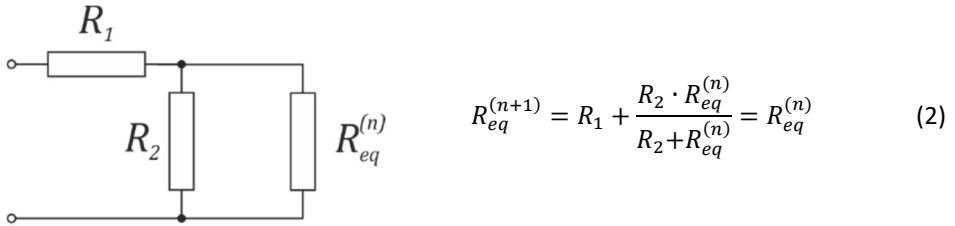
$$R_{eq}^{(n+1)} = R_1 + \frac{R_2 \cdot R_{eq}^{(n)}}{R_2 + R_{eq}^{(n)}} = R_{eq}^{(n)} \qquad (2)$$

Fig. 3 Adding an extra unit to the left of the ladder

If somebody will approach the semi-infinite ladder equivalent resistance by computer coding, the above listed equation will be useful for recursion.

When trying to solve Eq.2 for $R_{eq}^{(n)}$, one can find:

$$\left(R_{eq}^{(n)}\right)^2 - R_1 \cdot R_{eq}^{(n)} - R_1 \cdot R_2 = 0 \qquad (3)$$

with

$$R_{eq}^{(n=\infty)} = \frac{R_1}{2} \cdot \left[1 + \sqrt{1 + 4 \cdot \left(\frac{R_2}{R_1}\right)}\right] \qquad (4)$$

being the only positive root. This relationship is not depending on n, being a finite value determined only by the values of R_1 and R_2, and represent the correct solution to the problem of the equivalent resistance of a semi-infinite ladder.

The nodal voltages (U_k) and branch currents (I_k^s, I_k^p) are illustrated in Fig. 4:
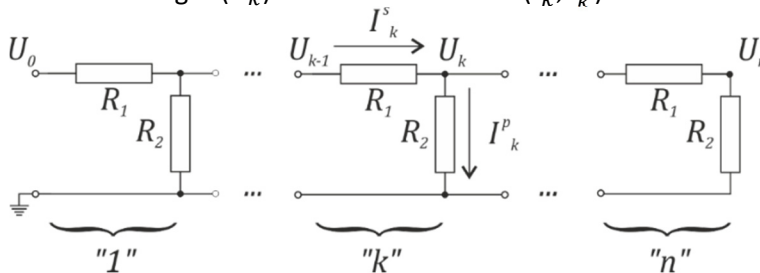
Fig. 4 Branch currents and nodal voltages along the ladder

15

By definition, the intensity of the currents in the series and parallel branches will be given by:

$$I_k^s = \frac{U_{k-1} - U_k}{R_1} \tag{5}$$

$$I_k^p = \frac{U_k}{R_2} \tag{6}$$

To find out an analytical expression for the nodal voltage U_k as function of both node position (k) and voltage existing at the previous node U_{k-1} or the input voltage U_0 is very laborious and will lead towards some very complicated looking polynomial ratios. The same is the situation if derive the transfer function A, representing the ratio between the voltage measured at the last node n and the input voltage U_0.

B. The particular case ($R_1 = R_2 = R$)

One of the most popular and mathematically beautiful particular case of the infinite or semi-infinite ladder is found when both resistors are equal in value because all the electrical characteristics of the ladder will be expressed by means of the Fibonacci numbers (F_n) or the golden ratio ($\varphi = 1.6180339887$) [27-29]:

$$F_n = \begin{cases} 0 \,, n = 0 \\ 1 \,, n = 1 \\ F_{n-1} + F_{n-2} \,, n \geq 2 \end{cases} \quad \text{with} \quad \lim_{n \to \infty} \frac{F_{n+1}}{F_n} = \varphi$$

In this case, the previously mentioned electrical parameters for the semi-infinite ladder, as function of the number of the (R_1, R_2) units, will become [30, 31]:

$$R_{eq}^{(n)} = R \cdot \frac{F_{2n+1}}{F_n} \tag{7}$$

$$U_k = \frac{F_{2(n-k)+1}}{F_{2n+1}} U_0 = \frac{F_{2(n-k)+1}}{F_{2(n-k)+3}} U_{k-1} \tag{8}$$

$$I_k^s = F_{2(n-k)+2} \cdot I_n^s \tag{5'}$$

$$I_k^p = F_{2(n-k)+1} \cdot I_n^p \tag{6'}$$

$$A = \frac{U_n}{U_0} = \frac{1}{F_{2n+1}} \tag{9}$$

C. A real case (1 $k\Omega$, ± 1 % tolerance resistors)

None the less, the results presented above are all "good looking" and leading towards predictable parameters, no one is tempted to move towards ladder design and experiment. Why? Because any experimental attempt regarding infinite or semi-infinite ladders seems to be overshadowed by two obstacles: (i) no one can build an infinite or semi-infinite circuit, even if uses tens of thousands or billions of resistors , (ii) cannot find resistors with exactly the same value except for those with very high precision (they are very expensive, a resistor with ± 0.1 % tolerance being significantly more expensive than one with a 1 % tolerance).

As a good compromise (acceptable tolerance for low price), let us consider, for simplicity in calculus, too … a batch of 1 kΩ, 0.5 W, 1 % tolerance resistors.

The worst-case scenario for design is when all resistors have resistances larger (or smaller) with exactly 1 %. If we consider the equivalent resistance of the semi-infinite ladder, given by Eq.4, to be function of R_1 and R_2, the uncertainty in $R_{eq}^{(n=\infty)}$, denoted $\Delta R_{eq}^{(\infty)}$, will be according to [32]:

$$\Delta R_{eq}^{(\infty)} = \sqrt{\left(\frac{\partial R_{eq}^{(\infty)}}{\partial R_1}\right)^2 \cdot \Delta R_1{}^2 + \left(\frac{\partial R_{eq}^{(\infty)}}{\partial R_2}\right)^2 \cdot \Delta R_2{}^2} \tag{10}$$

where

$$\frac{\partial R_{eq}^{(\infty)}}{\partial R_1} = \frac{\frac{1}{2} \cdot \sqrt{1 + 4 \cdot \left(\frac{R_2}{R_1}\right)} + \frac{1}{2} + \left(\frac{R_2}{R_1}\right)}{\sqrt{1 + 4 \cdot \left(\frac{R_2}{R_1}\right)}} \tag{11}$$

$$\frac{\partial R_{eq}^{(\infty)}}{\partial R_2} = \frac{1}{\sqrt{1 + 4 \cdot \left(\frac{R_2}{R_1}\right)}} \tag{12}$$

In the above listed relations $R_1 = R_2 = 1$ kΩ, $\Delta R_1 = \Delta R_2 =$ 0.01 kΩ.

Thus, the maximum uncertainty for the equivalent resistance in our case might be $\pm$ 0.011717 kΩ (11.717 Ω), meaning that any equivalent resistance value in the interval 1606.317 Ω and 1629.751 Ω, around the value given by the golden ratio (1618.034 Ω) , is acceptable.

What happens in a more realistic scenario, where the individual values of the resistors from the batch are spread around the value of 1 kΩ, but in the limit of the 1 % tolerance? We can estimate the level of uncertainty in the limiting net equivalent resistance, and obviously expect a narrower interval than that from the worst-case scenario.

If we have for the (R_1, R_2) units the mean values denoted $\langle R_1 \rangle$ and $\langle R_2 \rangle$ respectively, with small standard deviations σ_1 and σ_2, the uncertainty for the equivalent resistance will be given by

$$\sigma = \sqrt{\frac{\sigma_1^2 + \alpha^2 \cdot \sigma_2^2}{1 - \beta^2}} \tag{13}$$

$$\alpha = \left(\frac{R_2}{R_{eq} + R_2}\right)^2 \tag{14}$$

$$\beta = \left(\frac{R_{eq}}{R_{eq} + R_2}\right)^2 \tag{15}$$

This uncertainty will be calculated later in this paper, when discussing the experimental approach to the ladder, using real, commercially available resistors.

THE EXPERIMENTAL APPROACH TO THE RESISTIVE LADDER

In our opinion, it is not necessary to buy a tremendously large number of very good tolerance value resistors in order to construct and study an almost semi-infinite ladder, because as explained previously, the semi-infinite ladder has a finite equivalent resistance, and therefore, a not so large number of (R_1, R_2) units has to exist from where the equivalent resistance will converge, with an acceptable accuracy, to its value at infinity.

Coding is an excellent tool in order to find out such a value and has no difficulties with very large number of ladder units. We have developed a very simple Python code [33, 34] to find out the number of units (k) for which the equivalent resistance is still larger or equal to the golden ratio [29]. The recursive formula for

coding the equivalent resistance was adapted from Eq. 3, and a number of 10,000 units were initially targeted.

As one can see, surprisingly the condition for the equivalent resistance being larger or equal to the golden ratio is valid only for up to 15 units and the relative error becomes only 0.0626 % starting from the 4th unit. Thus, a semi-infinite ladder formed by identical resistors seems to be very short, nor longer than 15 units! Anyway, if trying to construct experimentally the ladder and make some experimental measurements, it would be useful and wise to consider a little bit larger number of units (20 in our case).

Although, according to the analytical and electric network analysis approach, the adding of a unit to the right end of the ladder is not correct and will not lead to the right solution. In our opinion, such an approach makes sense from experimental point of view: when building up a circuit, you start from the connection points (A and B, Fig.1), and add new units.

We have started to test our hypothesis using a digital multimeter (DMM) [35], a soldering breadboard [36] and 40 resistors (1 kΩ, 0.5 W, 1 %) [37]. The soldering type breadboard was preferred in order to avoid disturbing influences due to less perfect contacts. The randomly chosen pairs of R_1 and R_2 resistors were each measured and then successively mounted and soldered on the breadboard (Fig. 5). The equivalent resistance $R_{eq}^{(n)}$ was permanently monitored with the DMM.
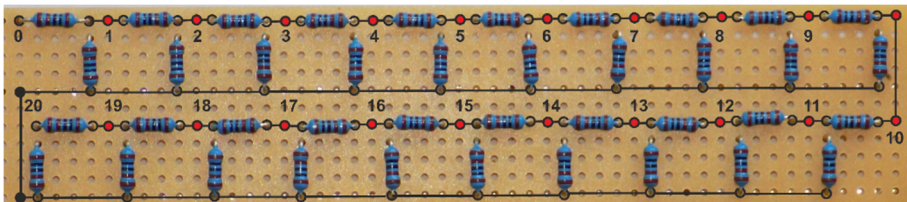
Fig. 5 A 20 units long resistive ladder on a soldering breadboard
(numbered points are measurement nodes; continuous line is the ground)

In order to have a sort of benchmark, a SPICE-based analog simulation program was used [38]. The results are depicted in Fig. 6.
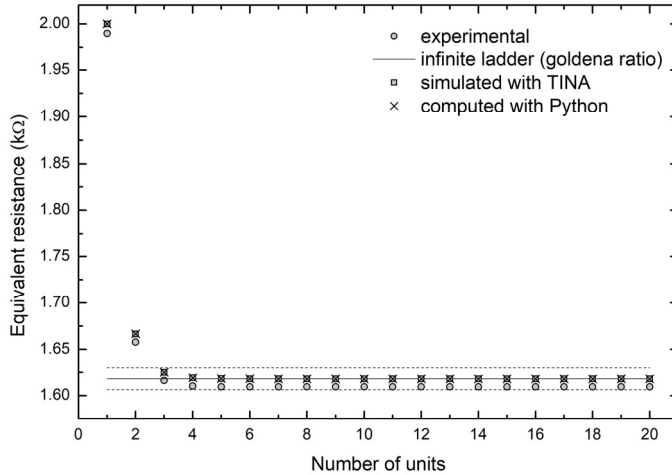
Fig. 6 Equivalent resistance of the ladder: experiment vs. theory

As one can see, and as it was expected, the convergence of the experimentally measured equivalent resistance is observed starting from the 4th unit (like in the case of coding), the relative error being around 0.48 % and the equivalent resistance being well inside the worst-case scenario interval (dashed lines), therefore our first hypothesis was confirmed. There is a good agreement between data, the measured equivalent resistances being smaller than the computed/simulated ones because the exact, real values of the purchased resistances used in our experiment were all less than 1 kΩ: $\langle R_1 \rangle = 0.99488$ kΩ, $\sigma_1 = 0.000891$ kΩ, $\langle R_2 \rangle = 0.99588$ kΩ, $\sigma_2 = 0.001298$ kΩ and $\sigma = 0.001031$ kΩ which is significantly less than the 0.011717 kΩ for the worst-case scenario.

Fig. 7 depicts the influence of the adding (or removing) order on the equivalent resistance. Firstly, the units were added to the right end, then they were removed from the right end. Finally, the 20-unit ladder was constructed again from the beginning and then the units were removed from the left end towards the 20th unit.

Fig. 7 validate and strengthen our second hypothesis regarding equivalent resistance: from experimental point of view it does not matter if you add or remove, from the so called "finite" or "infinite" end, the equivalent resistance will have the same dependence on the number of units and there is an excellent agreement between the different approaches.
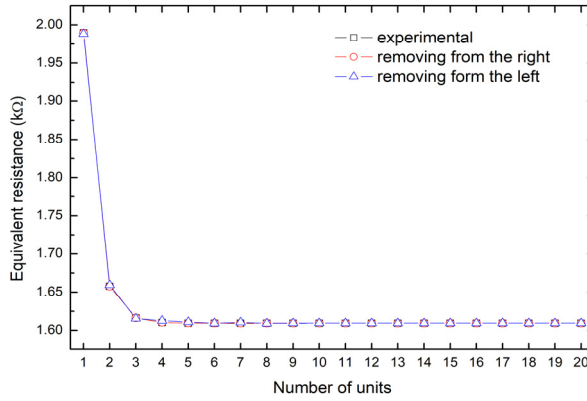
Fig. 7 Equivalent resistance evolution

Starting from the 14th unit the DMM used for measurements is not capable to reveal any changes in the value of the equivalent resistance, therefore experiment (more precisely the experimental apparatus accuracy) might "shorten" the ladder, probably to 14 units in our case.

According to the literature [4] an exponential decrease is expected for the currents in successive loops. In order to study this dependence, a programable DC power supply was used [39] to provide a steady 10 V input voltage (U_0), the nodal voltages being measured with the above mentioned DMM and the currents were calculated using the previously mentioned formulas (Eq.5 and 6). The voltage of each node and the branch currents are presented in Fig. 8, Fig. 9 and Fig. 10, respectively, the inserts representing the same plots, but on log-normal scale.
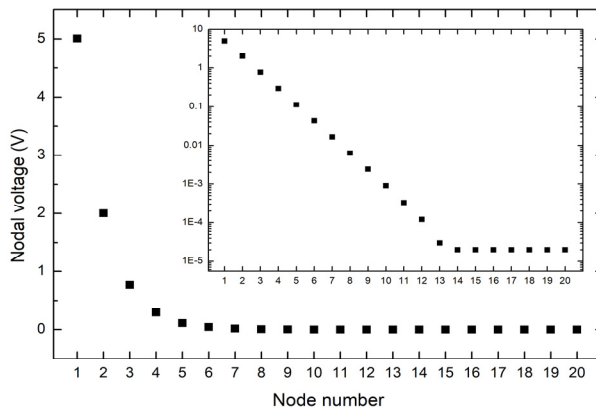
Fig. 8 Voltages measured in each node
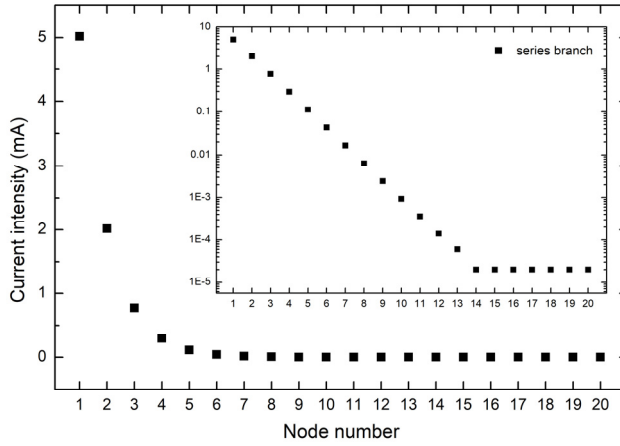
Fig. 9 Current intensity in series branches
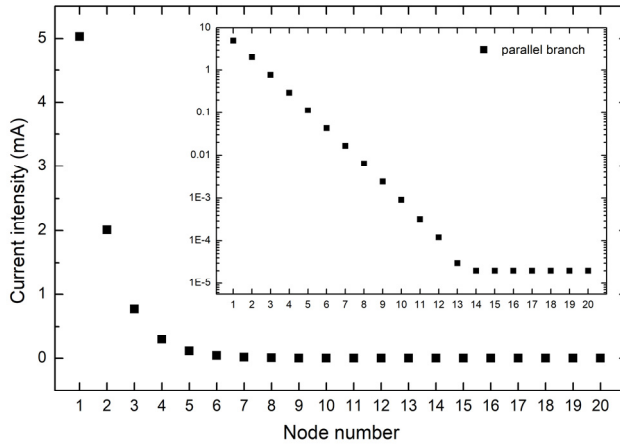
Fig. 10 Current intensity in parallel branches

As it was suspected by Denardo et al [4], voltage and currents present exponential decrease. Starting from node 14 the voltages are constant because the measurement precision of the DMM is exceeded and therefore are not reliable and appropriate for any scientific conclusions.

For the first 14 nodes, the evolution of the nodal voltages as function of the number of the (R_1, R_2) units is presented in Fig. 11, meanwhile Fig. 12 depicts the evolution of the relative error (as compared to theoretical value).
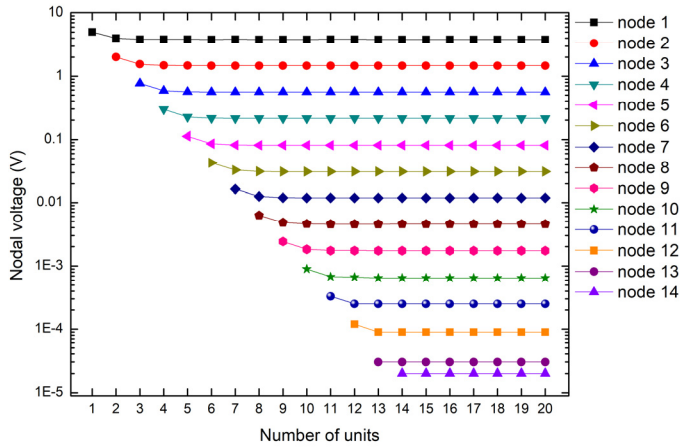
Fig. 11 Evolution of the nodal voltages as function of the number of units
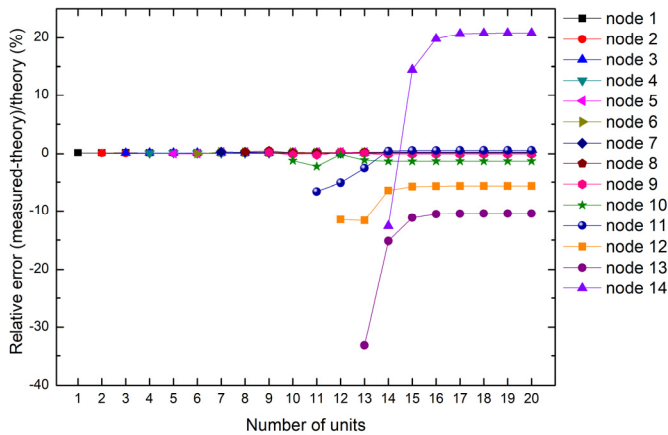
Fig. 12 Evolution of the relative error as function of the number of units

As one can observe on Fig. 12, the relative error become significant ($\geq$ 5%) starting from node 12 and unacceptable from here onwards. The branch currents deduced from the nodal voltages, for the first 12 nodes are presented in Fig. 13 (a) and (b).
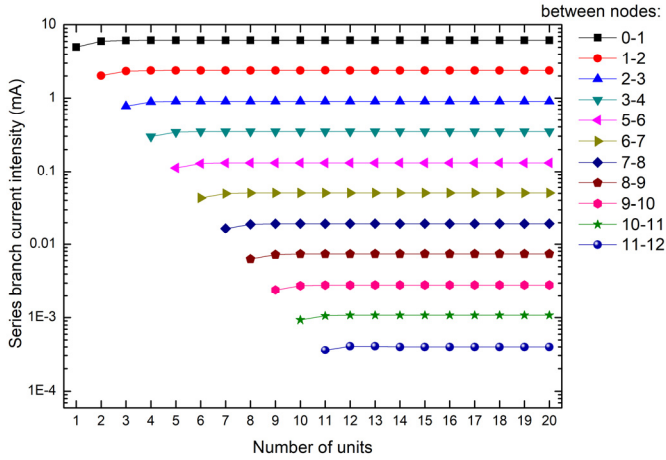
(a)
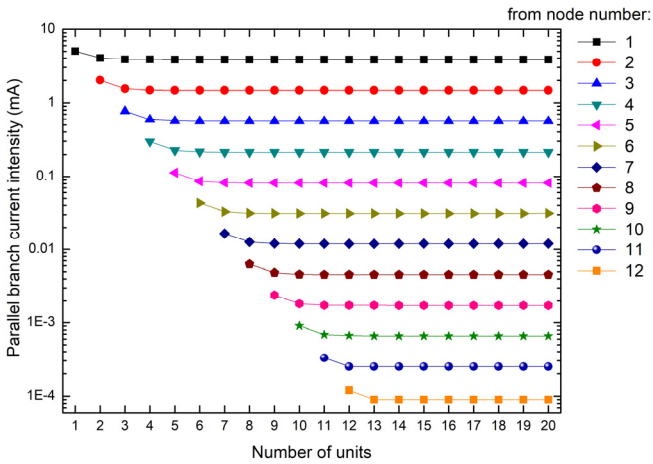
(b)

Fig. 13 Evolution of series (a) and parallel (b) branch currents
as function of the number of units

As demonstrated above, in both resistance or voltage measurements the experimental apparatus accuracy will "shorten" the ladder, down to 12 units in our case.

24

CONCLUSION

A semi-infinite resistive ladder was approached form both analytical and experimental (coding, simulation, measurements) point of views. It was demonstrated that in order to study the behavior of a such ladder it is not necessary to use a very large number of resistors: coding proved that the system tends to converge rapidly (only after about 15 units) towards a constant, finite value. This length of the ladder might be shortened by the accuracy of the experimental apparatus (digital multimeter) and experimental error. The results presented in this paper proved that from experimental measurement point of approach is doesn't matter which end of the ladder will be extended, the same steady, finite value will be reached.

ACKNOWLEDGEMENTS

<div align="center">

REFERENCES

</div>

1. D. Atkinson, F. J. van Steenwijk, *Am. J. Phys.* 67, 486 (1999)
2. A. H. Zemanian, *IEEE Trans. on Circuits and Systems*, 35 (11), 1346 (1988)
3. M. Jeng, *Am. J. Phys.*, 68, 37 (2000)
4. B. Denardo, J. Earwood, V. Sazonova, *Am. J. Phys.*, 67, 981 (1999)
5. A. Saggese, R. De Luca, *Eur. J. Phys.*, 35 (2014) 065006
6. R. H. March, *Am. J. Phys.*, 61, 900 (1993)
7. S. S. Sidhu, *Am. J. Phys.*, 62, 815 (1994)
8. D. Thompson, *Am. J. Phys.*, 65, 88 (1997)
9. F. J. van Steenwijk, *Am. J. Phys.*, 66, 90 (1998)
10. R. E. Aitchison*, Am. J. Phys.*, 32, 566 (1964)
11. F. J. Bartis, *Am. J. Phys.*, 35, 354 (1967)
12. L. Lavatelli, *Am. J. Phys.*, 40, 1246 (1972)
13. G. Venezian, *Am. J. Phys.,* 62, 1000 (1994)
14. H. A. Mavromatis, *Am. J. Phys.*, 63, 85 (1995)
15. C. H. Wörner, *The Physics Teacher*, 20, 477 (1982)
16. P. P. Ong, *The Physics Teacher*, 21, 459 (1983)
17. B. Scott, *The Physics Teacher*, 26, 578 (1988)

18. J. Higbie, *The Physics Teacher*, 35, 464 (1997)
19. T. P. Srinivasan, *Am. J. Phys.*, 60, 461 (1992)
20. R. M. Dimeo, *Am. J. Phys.*, 68, 669 (2000)
21. J. Cserti, *Am. J. Phys.*, 68, 896 (2000)
22. C. E. Mungan, T. C. Lipscombe, *Eur. J. Phys.*, 33, 531 (2012)
23. R. Beltrán, F. Gómez, R. Franco, J. A. Rodríguez, F. Fajardo, *Lat. Am. J. Phys. Educ.*, 7 (4), 621 (2013)
24. R. Ph. Feynman, R. B. Leighton, M. Sands, "The Feynman Lectures on Physics vol. II", Addison-Wesley Publishing Company, 1964, pp. 22-12–22-14
25. E. M. Purcell, "Electricity and Magnetism, Berkeley Physics Course - vol. 2", McGraw-Hill, New York, 1985, pp. 167–168
26. M. Kagan, X. Wang, arXiv:1507.08221v1 [physics.gen-ph] 10 Jul 2015
27. C. Bender, *The Fibonacci Quarterly*, 31 (3), 227 (1993)
28. A. M. Morgan-Voyce, *IRE Transactions on Circuit Theory*, 6 (3), 321 (1959)
29. Richard A. Dunlap, "The Golden Ratio and Fibonacci Numbers", World Scientific, 1997, Chapter 1-2, Chapter 4
30. A. D'Amico, M. Faccio, G. Ferri, *Il Nuovo Cimento D*, 12(8), 1165, (1990)
31. R. Lojacono, C. Falconi, G. Ferri, E. Lo Castro, M. Salmeri, A. Mencattini, M. Santonic, G. Pennazza, A. D'Amico, *World Journal of Research and Review (WJRR)*, 3 (6), 21 (2016)
32. J. R. Taylor, "An Introduction to Error Analysis, The Study of Uncertainties in Physical Measurements", University Science Books, USA, 1997, p. 75
33. G. Van Rossum, "The Python Language Reference Manual" Network Theory Ltd., 2003
34. http://atom.ubbcluj.ro/alpar/Extra/codes/
35. https://www.siglent.eu/siglent-sdm-3055.html
36. https://www.tme.eu/en/details/pc-01lam/universal-pcbs/sci/pc-1/
37. https://www.vishay.com/docs/28766/mbxsma.pdf
38. http://www.ti.com/tool/TINA-TI version Tina90-TI en.9.3.200.277
39. https://www.rigolna.com/products/dc-power-loads/dp800/

ON FLEXURAL PHONONS IN GRAPHENE.
THERMAL CONDUCTIVITY AND SPECIFIC HEAT

I. GROSU[1*] and M. CRISAN[1]

ABSTRACT. We analyzed the phonon spectrum of graphene. The flexural phonon contribution on thermal properties of graphene is discussed. The thermal conductivity has been calculated using the Boltzmann equation in the relaxation time approximation. The temperature dependence of the thermal conductivity and of the phonon specific heat has been calculated in the low temperatures domain.

Keywords: Graphene, Flexural phonons, Thermal conductivity, Specific heat

Phonons play a fundamental role in the physics and the characterization of graphene and carbon nanotubes. Phenomena as charge, spin, and heat transport, infrared and Raman spectra, electron-phonon scattering, and related effects as electric conduction can be understand, in most situations, by phononic spectrum. The simplest calculation of phononic spectra is based on the continuum elastic theory based on the known isotropy of the honeycomb lattice. Many experimental data as thermal conductance and specific heat have been explained using models of the harmonic theory for the lattice dynamics. In two dimensional (2D) systems the lattice long range order is destroyed by the thermal fluctuations, known as the Mermin-Wagner theorem [1-5], reconsidered for flexural phonons [6]. If the dynamics of lattice is treated in the harmonic approximation the concept of "phonon" is introduced and used to describe the thermal properties [7]. Although the exact dispersion law of the acoustic modes is apparently irrelevant in the quantified thermal conductance [8], the quadratic dispersion of the flexural modes is important in describing the low-temperature specific heat [9]. Most of the results [10-12] cover a wide temperature interval and provide approximative estimation of the power low of the T-dependence, but only few works [9, 13] extended the temperature

range down to 0.1 K and provide a more precise analysis and proposed $C(T) \sim T^{1/2}$. The out-of-plane distortions, called flexural phonons, are important for the theory of transport in graphene because of the anharmonicity effect [14, 15]. The anharmonic coupling of flexural phonons to the in-plane modes give the stable 2D graphene to rippling. An important effect of anharmonicity is the enhancement of dispersion relation of the long- wavelength flexural modes. The effect of anharmonicity has been considered by Mariani and von Oppen [17] using an effective energy functional including corrections to the harmonic potential that are lowest order in the wave vector, which then couple to flexural modes. Using the Renormaliztion Group (RNG) method they calculated the energy of the flexural modes on the continuum model. The main result is the modification of the dispersion dependence from $\omega \sim q^2$ at low temperatures, to $\omega \sim q^{3/2}$ at high temperatures. In this paper we concentrate on the contribution of the flexural phonon on the thermal properties of graphene.

The mechanical distortions of graphene are described by the vector **u(r)** by the scalar h(**r**) associated with in-plane and flexural (out-of-plane) deformations, respectively. The physics of mechanical distortions is captured in the elastic Lagrangian density. In the harmonic approximation the Lagrangian yields two in-plane phonons modes, longitudinal (*l*), transverse (*t*) and one flexural branch (*f*) with dispersions

$$\omega_l(q) = v^l q \tag{1}$$

$$\omega_t(q) = v^t q \tag{2}$$

$$\omega_f(q) = \sqrt{((\gamma \, q^2 + \kappa \, q^4)/\rho)} \tag{3}$$

and group velocities $v^l = [(2\mu + \lambda)/\rho]^{1/2}$ $v^t = [\mu/\rho]^{1/2}$. The flexural branch has a quadratic dispersion in the absence of external strain and introduce a new vector scale $q_s = [\gamma/\kappa]^{1/2}$ discriminating a strain-induced linear dispersion

$$\omega_f(q) \simeq [\gamma/\rho]^{1/2} q \equiv v^f q \tag{4}$$

where $\gamma = 2u(\mu + \lambda)/\rho$, u being the strain, for $q \ll q_s$, and

$$\omega_f(q) \simeq [\kappa/\rho]^{1/2} q^2 \tag{5}$$

for $q \gg q_s$. In the absence of strain: $v^l \simeq 21 \ km/s$, and $v^t \simeq 14 \ km/s$. There is no agreement for v^f but near the Brillouin zone boundary: $v^f \simeq 8 \ km/s$. The flexural phonons dominate the phonon contribution in resistivity [17], and the divergence

in scattering rate is logarithmical if the quadratic dispersion of flexural phonons is considered. This divergence is cut off by coupling between bending and stretching degrees of freedom contained in the Lagrangian. At finite temperature, this coupling reorganize the bending rigidity including a stiffening of the flexural dispersion at long wavelength. The energy of flexural phonons $\omega_f(q)$ is modified by this interaction and in lowest order is

$$\omega_F^2(q)= \omega_f^2(q)+ \Re\,\Sigma(\omega_f(q))/\rho \tag{6}$$

In the high-temperature limit, the self-energy $\Sigma(\omega_f(q))$ has been calculated by Amorim et al. [16] as

$$\Re\,\Sigma(\omega_f(q))= C\,k_B T\,q^2 \tag{7}$$

where C depends on μ and λ. The energy can be approximated in terms of temperature momentum scale $q_c^2= (\gamma+ C\,k_B T)/\kappa$ as

$$\omega_F(q)= \alpha_0\left[1+\frac{q_c^2}{q^2}\right]^{1/2} q^2 \tag{8}$$

where $\alpha_0= \sqrt{\kappa/\rho}$. This expression can be approximated as:

$$\omega_F(q)\simeq\alpha_0\, q^2 \tag{9}$$

for $q > q_c$, and:

$$\omega_F(q)\simeq\alpha_0\, q_c\, q \tag{10}$$

for $q < q_c$. Mariani and von Oppen [17] studied the effect of anharmonicity on the flexural modes starting with the energy of nearly flat graphene, including lowest order corrections to the harmonic potential which couple the flexural modes to the in-plane modes. Following the RNG strategy they intergraded out the in-plane modes leaving an effective temperature-dependent interaction among the flexural modes. In the one-loop approximation the energy of flexural modes was calculated as

$$\omega_F(q)= \alpha_r(T, q)\, q^2 \tag{11}$$

where

$$\alpha_r(T,q)= \alpha_0\left[1+\frac{\bar{q}_c^2}{q^2}\right]^{1/4} \tag{12}$$

and q_c is $T^{1/2}$ dependent. These results show that $\omega_F(q) \sim q^2$ at low temperatures, while $\omega_F(q) \sim q^{3/2}$ at high temperatures, which is different to the linear dependence given by Eq.(10). This difference is given by the simple correction to the flexural energy $\omega_F(q)$ given by the self- energy term. We mention that the quadratic dispersion is important because it gives a constant density of states for phonons, but the linear dependence lead to a linear energy dependent density of states. The $q^{3/2}$ dispersion has been proposed in a phenomenological model by Jacimovski et al. [18] for calculation of the thermal conductivity of graphene. This dispersion is supposed to be more realistic than the q-dependence in the temperature interval 15K- 400K, and it is agrement with experimental data.

The phonon thermal conductivity is determined from Boltzmann transport equation as

$$K(T)=\frac{1}{(4\pi h k_B T^2)}\int_{q_m}^{q_M} q\,dq\,\Omega^2(q)\tau_F \frac{\left(\exp\left(\frac{(\hbar\omega_F(q))}{(k_B T)}\right)\right)}{\left(\exp\left(\frac{(\hbar\omega_F(q))}{(k_B T)}\right)-1\right)^2}$$

(13)

where $\Omega(q)= \hbar\omega_F(q)\dfrac{(d\,\omega_F(q))}{dq}$, h – the thickness of graphene, and I_F is the phonon scattering rate, which is given by different contributions. Klements and Pedraza [19] developed a model for the scattering rate considering the intrinsic phonon-phonon scattering, taking for the three-phonon scattering processes rate

$$\frac{1}{\tau_F}= \gamma_s^2 \frac{(k_B T)}{(Mv^2)}\frac{\omega^2}{\omega_D}.$$

(14)

where γ_s, M and ω_D are the Gruneisen parameter, the mass of an atom, and the maximum frequency of the acustic mode in the Debye approximation respectively. v represent the average phonon velocity. Nika et al. [20] calculated the scattering rate considering three-phonon scattering that satisfy momentum and energy conservation. Linsday et al. [21] considered the three-phonon scattering processes involving the flexural modes with an even number of phonons, neglecting the four-scattering processes, considered by De Martino et al. [22], and Feng and Ruan [23]. The recent analysis from [23] suggested that four-scattering processes, quadratically dependent with temperature, are more important than the three-scattering processes.

In order to calculate the contribution of the flexural phonons to the thermal conductivity we use $\omega_F(q) = \alpha_0\, q^2$ valid in the low temperature case. To calculate the temperature dependence of the thermal conductivity we consider the scattering time as: $\tau_F = A\,\omega_F^{-2}\, T^{-\gamma}$ (see also, Lindsay et al. [21]), and using $\hbar\omega_F = x\, k_B T$, Eq.(13) becomes

$$K(T) = \frac{(A k_B T^{-\gamma})}{(2\pi h)} \int_{\Theta_m/T}^{\infty} dx\, \frac{(x e^x)}{(e^x - 1)^2}$$

(15)

where $\Theta_m = \hbar\omega_m / k_B$. The integral from Eq.(15) can be analytically performed and we get

$$K(T) = \frac{(A k_B)}{(2\pi h)} \left(\frac{1}{T}\right)^{\gamma} \left[\frac{(\Theta_m/T)}{(e^{\Theta_m/T} - 1)} - \ln\left(1 - e^{-\Theta_m/T}\right) \right]$$

(16)

which can be approximated as

$$K(T) \simeq \frac{(A k_B)}{(2\pi h)} \left(\frac{1}{T}\right)^{\gamma} \frac{\Theta_m}{T} e^{-\Theta_m/T}$$

(17)

The contribution to specific heat of the phonons is given by:

$$C_p = \int_0^{\omega_{max}} k_B \left(\frac{(\hbar\omega)}{(k_B T)}\right)^2 \frac{e^{\hbar\omega/k_B T}}{(e^{\hbar\omega/k_B T} - 1)^2} \rho(\omega)\, d\omega$$

(18)

The specific heat temperature dependence is sensitive to characteristics of the phonon spectrum and on its density of states [24, 25]. In the case of low temperatures we use the energy of the flexural phonons given by $\omega \equiv \omega_F \simeq \alpha_0 q^2$, which gives the density of states: $\rho \simeq 1/4\pi\alpha_0$. In this case the specific heat is calculated from Eq.(18) as:

$$C_p(T) \simeq \frac{(\pi k_B^2 T)}{(12\,\alpha_0\, \hbar)}$$

(19)

We presented an analytical theory of the flexural phonon contribution on thermal properties of graphene. The continuum elasticity approach giving the flexural modes with dispersion $\omega_F(q) \sim q^2$ has been discussed, using the renormalization

group method [17], to include the anharmonicity of the dispersion relation in the long-wavelength flexural modes. The q-dependence of the dispersion $\omega(q)$ has a temperature dependence, at low temperatures as $\omega(q) \sim q^2$ and at high temperatures as $\omega(q) \sim q^{3/2}$. The thermal conductivity has been calculated using the Boltzmann equation along with the relaxation time approximation. The linear ($\gamma = 1$) and quadratic temperature dependence ($\gamma = 2$) in relaxation time, given by three-phonon and four-phonon processes have been considered. The temperature dependence of the thermal conductivity $K(T)$ is affected by the dispersion $\omega(q)$ and the scattering rate I_F. The temperature dependence of dispersion appears due to the anharmonicity effect considered in Ref.[22], but the temperature dependence of scattering rate was introduced phenomenologically [21], or estimated theoretically considering the phonon-interaction[22,23]. Using the RNG results we obtained $K(T) \sim T^{-\gamma-1} \exp(-1/T)$ in the low temperatures limit, where $\gamma = 1,2$ for three, respectively four phonon processes. At low temperatures the phonon specific heat scales as $C_p \sim T^{d/2}$, for a phonon dispersion $\omega \sim q^2$, in d-dimensions [9,26]. We obtained that the specific heat $C_p(T)$, which is sensitive to dispersion, is linear in the low temperatures domain $C_p(T) \sim T$. These results could be of interest in low dimensional graphene systems, and could be extended to other properties of graphene and graphene layers, such as the superconductivity of graphene layers at magic angle [27] (with associated properties [28-30]).

REFERENCES

1. N.D. Mermin, H. Wagner, *Phys.Rev.Lett.,* 17, 1133 (1966)
2. P. C. Hohenberg, *Phys. Rev.,* 158, 383 (1967)
3. S. Coleman, *Comm. Math. Phys.,* 31, 259 (1973)
4. R. E. Peierls, *Ann. I. H. Poincare,* 5, 177 (1935)
5. L. D. Landau, *Phys. Z. Sowjetunion,* 11, 26 (1937)
6. M. V. Fischetti, W. G. Vandenberghe, *Phys. Rev. B*93, 155413 (2016)
7. A. H. CastroNeto, F. Guinea, N. M. R. Peres, *Rev. Mod. Phys.,* 81, 109 (2009)
8. N. Mingo, D. A. Broido, *Phys. Rev. Lett.,* 95, 96105 (2005)
9. V. N. Popov, *Phys. Rev. B*66, 153408 (2002)
10. A. Mizel, L. Benedict, M. Cohen, S. Louie, A. Zettl, N. Budraa, W. Beyermann, *Phys. Rev. B*60, 3264 (1999)

11. E. Dobardzic, I. Milosevic, T. Vukovic, M. Damnjanovic, *Phys. Rev. B*68, 45408 (2003)
12. C. Li, T. -W. Chou, *Phys. Rev. B*71, 75409 (2005)
13. J. C. Lasjaunias, K. Biljakovic, Z. Benes, J. E. Fischer, P. Monceau, *Phys. Rev. B*65, 113409 (2002)
14. K. V. Zakharchenko, M. I. Katsnelson, A. Fasolino, *Phys. Rev. Lett.,* 102, 046808, (2009)
15. K. V. Zakharchenko, R. Roldan, A. Fasolino, M. I. Katsnelson, *Phys. Rev. B*82, 125435, (2010)
16. B. Amorim, R. Roldan, E. Cappelluti, A. Fasolino, F. Guinea, M. I. Katsnelson, *Phys. Rev. B*89, 224307 (2014)
17. E. Mariani, F. vonOppen, *Phys. Rev. Lett.* 100, 076801, (2008); *Phys. Rev. Lett.* 100, 249901(E) (2008)
18. S. K. Jacimovski, M. Bukurov, J. P. Setrajcic, D. J. Rakovic, *Superlat. and Microst.,* 88, 330 (2105)
19. P. G. Klemens, D. F. Pedraza, *Carbon,* 32, 735 (1994)
20. D. L. Nika, E. P. Pokatilov, A. S. Askerov, A. A. Balandin, *Phys. Rev. B*79, 155413 (2009)
21. L. Lindsay, D. A. Broido, N. Mingo, *Phys. Rev. B*82, 115428 (2010); *Phys. Rev. B*83, 235428 (2011)
22. A. DeMartino, R. Eigger, A. O. Gogolin, *Phys. Rev. B*79, 205408, (2009) 23. T. Feng, X. Ruan, *Phys. Rev. B*93, 045202 (2016)
24. L. Rego, G. Kirczenow, *Phys. Rev. Lett.,* 81, 232 (1998)
25. J. Hone, B. Batlogg, Z. Benes, A. T. Johnson, J. Fischer, *Science,* 289, 1730, (2000); J. Hone, M. C. Llaguno, M. J. Biercuk, A. T. Johnson, B. Batlogg, Z. Benes, J. Fischer, *Appl. Phys. A*74, 339 (2002)
26. E. Pop, V. Varshney, A. K. Roy, *Mater. Res. Soc. Bull.,* 37, 1273 (2012)
27. T. J. Peltonen, R. Ojajärvi, T. T. Heikkilä, *arXiv:* 1805. 01039
28. P. B. Allen, B. Mitrovic, *"Solid State Physics"* edited by H. Ehrenreich, F. Seitz, D. Turnbull, Academic, New York (1982)
29. B. Krunavakarn, P. Udomsamuthirun, S. Yoksan, I. Grosu, M. Crisan, *J. Supercond*., 11, 271 (1998)
30. D. C. Mattis, M. Molina, *Phys. Rev. B,* 44, 12565 (1991)

INSTALLATION FOR SHORT TIME HEAT TREATMENT
AT HIGH TEMPERATURE

R. HIRIAN[1*]

ABSTRACT. The design of a simple installation for short time annealing of nanomaterials at high temperature is presented. The installation is capable of heating rates of over 20 °C/s and cooling rates of up to 80 °C/s with a maximum attainable temperature of 1050 °C.

Keywords: *short time annealing, temperature measurement, controlled atmosphere, high heating rate*

INTRODUCTION

Many scientific efforts today focus on nanomaterials and nanostructured materials [1-3]. Some of these materials need to be annealed in order to tune their structure and/or microstructure; however annealing processes must be short in order to maintain the desired length scales [4-6]. Therefore it is essential to reach the annealing temperature as fast as possible and then quench the samples as fast as possible. To this end we have constructed an installation capable of heating rates of up to 20 °C per second and cooling rates of over 80 °C per second. Therefore a sample can be heated to 950 °C and brought back to room temperature in 65 s.

EXPERIMENTAL

The annealing instalation consists of a furnace, quartz tube, vacuum and gas system and temperture sensor.

[1*] *Faculty of Physics, Babeş-Bolyai University, Cluj-Napoca, RO-400084 Romania,*
  Hirian.Razvan@ubbonline.ubbcluj.ro

The furnace is a small carbolite tube furnace with a maximum temperature of 1200 °C. The homogenious heating area of the furnace is 5 cm.

The quartz tube is used as the sample chamber, as quartz has great thermal shock resistance and can withstand high vacuum. For our specific tubes, the vitrous transistion was found to be at aproximately 1100 °C, therefore heating was limited to 1050 °C in our case to avoid melting the tube.

The vacuum system consists of a Pfeifer turbo pumping station isolated which can be isolated with a gate valve. The gas system is also isolated from the tube system by a valve, therfore we can easly switch between gas and vacuum. The gas system has a purge chamber, equipped with an oxigen sensor, so that the gas can be run trough it until the O_2 concentration falls below 2 ppm. The O_2 sensor also monitors oxigen levels during annealing.
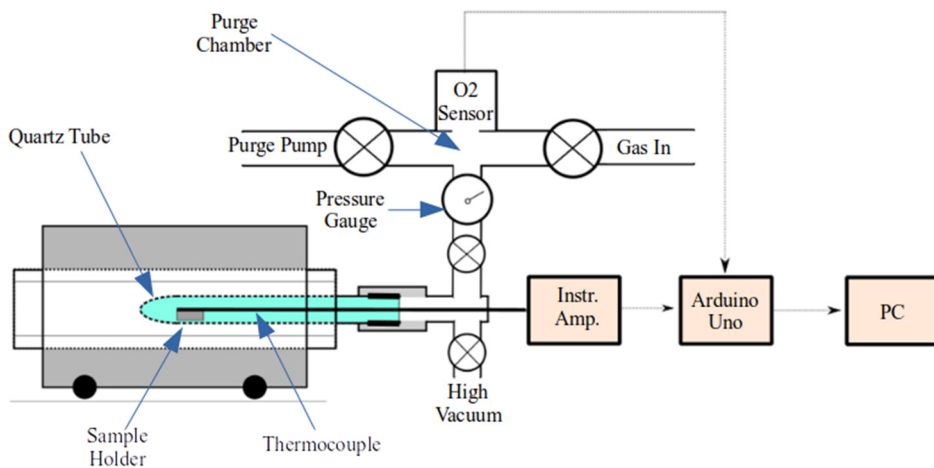
Fig. 1 Schematic Representation of Annealing Installation

For the temperature measurement, an S-type thermocouple has been passed trough a air tight meatal plate (sealed with epoxy) and afixed to the sample holder (a thin tantalum cilinder). As S-type thermocouples give a low voltage signal, the output is amplified by a simple instrumentation amplifier using the LM358N operational amplifier chip. The amplified signal is then read by an Arduino Uno [7] microcontroller board and transmited to a Raspberry Py 2 [8]. In order to reduce most of the electronic noise, an averege is taken every 100 measurements. As the arduino chip does not have a timekeeping function, after setting up the measurement

loop we let it measure for an hour and calculated the time per cycle in order to determine the time in seconds. The computer software (writen in Python [9]) takes the output from the arduino and converts it intro physical values which it writes to a data file. The accuracy of the temperature measurement is limited to ±2 C. Real time data monitoring is done with Gnuplot [10].

The instalation functions by inserting the prepared quartz tube into the pre-heated furnace.

RESULTS AND DISCUSSION

The performance of the setup was tested in high vacuum (10^{-5} mbar), high purity He and high purity Ar atmosphere. Heating and cooling rates are shown in Fig 2.

Of course, the heating and cooling rates are slow in high vacuum, even when the quartz tube is immersed in cold water Fig. 2a, 2b and 2c. The introduction of Ar gas significantly improes the heating and cooling speed, however the rates are not linear. Switching to He gas does little to improve the heating rate, however quenching is much faster in this configuration. The lack of a significant benefit when using He while heating is very likely due to the large mass and thermal inertia of the quartz tube, which is less of a factor when it is plunged in cold water. Preheating the tube as well, and inserting the samples with a thin manipulator rod might improve preformance signiicantly.

a)

b)
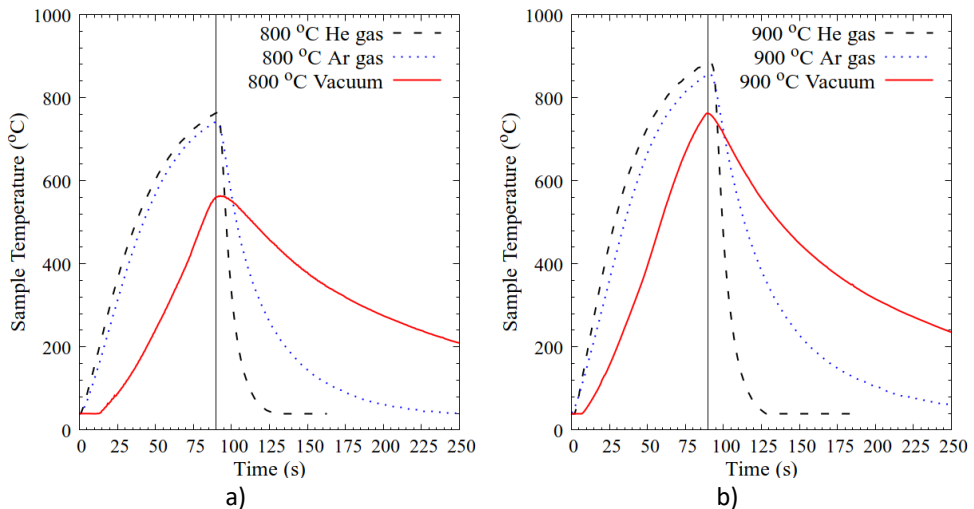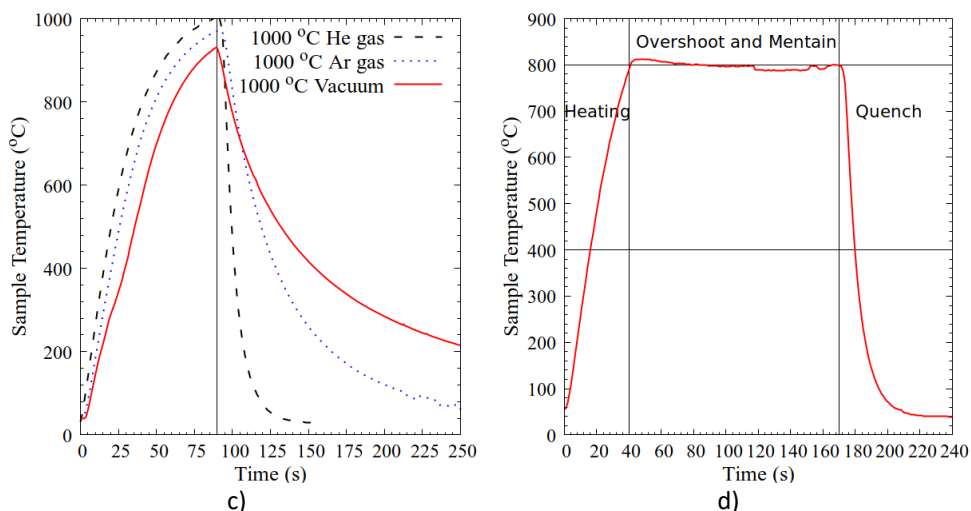
Fig. 2 Example heating and cooling curves with the furnace pre heated to a) 800, b) 900 and c) 1000 °C and an example heating and holding curve d)

We should also note the shape of the heating curves, it is only natural that our heating rates go down as we approach the set temperature of the furnace, therefore we see a much steeper curve at low temperature when compared to high temperature, still we can achive avereg heating rates of about 20 °C/s up to 900 °C, which is not insignificant. The setup is capable of reaching 950 °C in 65 s, 900 °C in 50 s, 800 °C in 38 s and 700 °C in 27 s etc. Fig. 2c. The cooling speed is aproximately 80 °C / s when using He as the heat transfer gas.

Some ramp and hold annealings can also be performed, Fig. 2d, by changing the sample position inside the furnace. However this procedure induces a temperature gradient of about 5 °C, and is very hard to execute as swift and precise movements of the furnace are required.

CONCLUSSIONS

A rapid annealing instalation capable of avereg heating and cooling rates of 20 °C/s and 80 °C/s respectively, was constructed. The setup can run under high vacuun, purified Ar or He gas atmosphere and the oxigen concentration (when gas is used) can be monitored during the annealing process.

Future modificantions which could improve heating rates could consist of: (i) a thin manipulator arm for inserting the sample at high temperature, (ii) replacing the quartz tube with one with a higher melting point so that the furnace set temperature can be increased, (iii) lowering the He pressure to improve heat transfer from the tube to the samples and therfore increase the cooling rates.

ACKNOWLEDGMENTS

REFERENCES

[1] A. Hosokawa, K. Takagi, T. Kuriiwa, *J. Magn. Magn. Mater.*, 439, 220-227 (2017)
[2] D. Reichel, W. Skorupa, *Phys. Status. Solidi. C,* 9, 2045-2049 (2012)
[3] J. Xu, Z. Hu, X. Jia, L. Huang, X. Huang, L. Wang, P. Wang, H. Zhang, J. Zhang, J. Zhang, Y. Zhu, *Org. Electron.*, 34, 84-90 (2016)
[4] E. F . Kneller, R. Hawing, *IEEE Trans. Magn.*, 27, 3588-3600 (1991)
[5] V. Pop, S. Gutoiu, E. Dorolti, O. Isnard, I. Chicinas*, J. Alloy. Compd.,* 509, 9964-9969 (2011)
[6] R. Hirian, S. Mican, O. Isnard, L. Barbu-Tudoran, V. Pop, *, J. Alloy. Compd.,* 697, 19-24 (2017)
[7] https://www.arduino.cc/ (last accessed Dec, 2019)
[8] https://www.raspberrypi.org/ (last accessed Dec, 2019)
[9] https://pypi.org/project/pyserial/ (last accessed Dec, 2019)
[10] http://www.gnuplot.info/ (last accessed Dec, 2019)

LOW-COST, LOAD CELL AND MICROCONTROLLER BASED BENDING STIFFNESS TESTER

Z. KAPUSI[1], A. TUNYAGI[2] and A. SIMON[2*]

ABSTRACT. Paper and paperboard have many applications, from writing, printing and householding to packaging. Bending stiffness is probably the most important mechanical property of paper and paperboard, it provides rigidity in some industrial processes like printing or folding. The present work describes the design and implementation of a low-cost bending stiffness tester proposed as a graduation project for Engineering Physics students. The performances of the device were successfully tested on both certified and real-life paper products.

Keywords: bending stiffness, paper products, strain gauge, load cell, stiffness tester

INTRODUCTION

Bending stiffness is very important for the paperboard-based packaging industry, therefore various methods and devices were proposed to measure such a characteristic. The topic is a complex one, from both theoretical and experimental point of views and giving an excellent inter- and multidisciplinary subject for Engineering Physics undergraduate students.

This work describes the implementation of a low-cost bending stiffness tester proposed as a graduation project for Engineering Physics specialization, at Babeș-Bolyai University, Faculty of Physics [1]. The paper is organized as follows: in the first section the general properties of paper and paperboard are briefly presented, with emphasis on stiffness and measuring principles, the design, implementation and calibration processes are described in the subsequent sections and finally, the measurement results made on some commercially available paperboard-based food packages are also presented.

---

[1] *Undergraduate student, Engineering Physics*

[2] *Babeș-Bolyai University, Faculty of Physics, M. Kogălniceanu 1, 400084 Cluj-Napoca, Romania*

* Corresponding author: alpar.simon@phys.ubbcluj.ro

THE BENDING STIFFNESS OF PAPER PRODUCTS AND ITS MEASUREMENT

Paper and paperboard have many applications, from writing, printing and householding to packaging. Paper is a relatively thin material (usually less than 0.3 mm) produced by filtration of a cellulose pulp (suspension) followed by pressing and drying, meanwhile paperboard is thicker (usually over 0.30 mm), has a more complex structural construction and consequently a better foldability and rigidity [2, 3].

Due to characteristics of the processing technologies and the fact that cellulose fibers are much longer than thick, the fibers become oriented more or less in the plane of the paper. Therefore, paper becomes a layered structure, but with a certain anisotropy. The preferred orientation of the cellulose fibers is called machine direction (MD) because it is determined by the hydrodynamic forces present in the papermaking process. The in-plane direction perpendicular to this preferred direction is called the cross machine (CD) direction, meanwhile the off plane perpendicular direction is called the thickness direction (ZD) [4].

The resistance of an object to a mechanical action is called stiffness. If this action tends to bend the object, we call the response bending stiffness. According to the most generally accepted methods of stiffness measurements, bending stiffness is the measure of the force which has to be applied in order to bend a piece of material through a given distance or angle. Bending stiffness is probably the most important mechanical property of paper and paperboard, it provides rigidity in some industrial processes like printing or folding. A certain level of bending stiffness of the paperboard is required in converting, packaging, transportation, storing and handling of paperboard-made packaging products. The soft, less rigid paper products used in householding (tissues and towels) have low bending stiffness, a high stiffness is required for newspaper in order to avoid falling together or bending under its own weight. Paper-based food packages, boxes and sacks requires high stiffness to reduces the tendency of buckling when their content presses against walls.

In paper industry, bending stiffness (S_b, measured in mN·m units) is defined as the moment of the resistance, per unit width that a paper or board present against bending within the limits of elastic deformation [4] or as the bending moment, per unit width of a rectangular test paper divided by the curvature [5]:

$$S_b = \frac{EI}{b} \qquad (1)$$

$$S_b = \frac{M}{bc} \qquad (2)$$

where E is the Young modulus of the paper, I is the second moment of area (moment of inertia) of the cross/sectioned area about an axis through the center of that area, perpendicular to the direction of bending, b is the width of the cross section area considered, M is the bending moment (force x its arm), c is the curvature (inverted value of the bending radius)

There are several well proven techniques for measuring bending stiffness: namely resonance, two-point, three-point and four-point method. All these methods are well documented and described in literature [3-8] and there are several standardized, commercially available bending stiffness measuring devices [9-14]. All of them were designed for industrial use, consequently their market price is relatively high.

The resonance method (Fig. 1a) is based on the determination of the length at which a paper strip will come into forced resonance. The strip of paper or paperboard is held vertically in a clamp vibrating at a fixed frequency. The free length of strip projecting above the clamp will undergo forced vibration. This free length is adjusted for resonance condition (visually recognizable as maximum vibrational amplitude of the free end). The free length of the strip at which resonance occur, is measured. It is called resonance length and is related to bending stiffness (S_b, in mN·m) by the following relationship:

$$S_b = 3.19 \cdot 10^{-12} \cdot l^4 \cdot w \cdot f \tag{3}$$

where w is the grammage or paper density (in g/m^2), f is the vibration frequency (in Hz) and l is the resonance length (in mm).
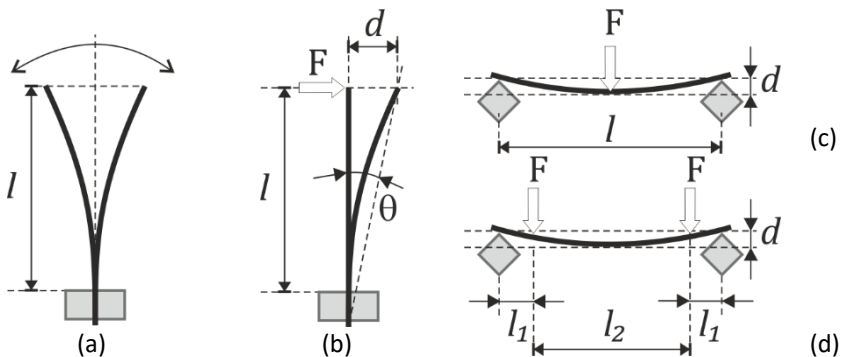
Fig. 1 Bending stiffness determination by: (a) resonance method, (b) two-point method, (c) three-point method, (d) four-point method

The stiffness of lightweight or thin materials is measured by applying a force (F) to the free end of a fixed size piece of the material having length (l), which is clamped at the other end, and deflecting the free end through a fixed distance (d) or angle (θ). This is the two-point method (Fig.1b). For heavyweight or thick materials, the two-point method could cause crushing, even at low-bending angles, which results in anomalously low stiffness values. For these materials, the three-point (Fig.1c) or the four-point (Fig.1d) methods are preferred.

The bending stiffness (S_b, in mN·m) is given by the following relationships:

two-point method: $$S_b = \frac{60Fl^2}{b\theta\pi} \quad (4) \qquad \text{and} \qquad S_b = \frac{Fl^3}{3db} \quad (5)$$

three-point method: $$S_b = \frac{Fl^3}{48db} \quad (6)$$

four-point method: $$S_b = \frac{Fl_1\, l_2^2}{3db} \quad (7)$$

where F is the bending force (in N), l is the test length or bending length (in mm), b is the test width (in mm), d is the deflection (in mm) and θ is the angular deflection (in degrees), l_1 (in mm) is the distance between the outer support and its nearer inner support and l_2 (in mm) is the distance between the inner supports.

Regardless of the applied technique, due to the anisotropic structure of the paper, bending stiffness has to be determined in both MD and CD directions. The MD stiffness value is always higher than the CD value. Stiffness ratio (i.e. MD stiffness/CD stiffness) is a very commonly used indicator of the anisotropy of the paper product (rarely, the geometric means stiffness, i.e. the square root of the product of the two stiffnesses is used).

FORCE MEASUREMENT

The values of the quantities used in the above-mentioned methods (angle, length, dimensions, deflection) are given by international standards and excepting the resonance method, all techniques require force measurement.

A very convenient force measurement method uses strain gauges. A strain gauge (Fig. 2) is a passive transducer whose relative electrical resistance varies in proportion to the amount of strain in the device [15]. Usually, it consists of a very fine wire or metallic foil arranged in a grid pattern bonded on a thin supporting foil (carrier).
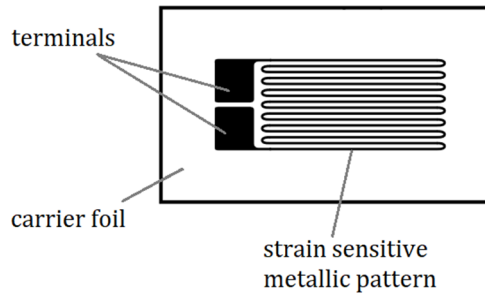
Fig. 2 Metallic strain gauge

Although, the first investigations about the changes of resistance caused by the strain in wires were made in the 1850's [16], the strain gauges were invented almost same time only in the late 1930's and patented in mid-1940's, the by E.E. Simmons [17] and A.C. Ruge [18]. Simmons was investigating the stress–strain behavior of metals under shock loads, while Ruge investigated the influence of earthquakes on mechanical structures.

Strain gauges are available commercially with nominal resistance values from 30 to 3000 Ω, with 120, 350 and 1000 Ω being the most common values [19].

There are several disadvantages in the use of stand-alone strain gauges: difficulty in manipulation, the relative change in resistance cannot be measured directly, low sensitivity, influence of temperature variations and thermal expansion, etc.

In order to avoid those disadvantages, load cells were developed. A load cell is a force sensing module, a transducer taking as input a force and converting it at the output into an electrical signal (voltage). It is consisting of a specially designed aluminum structure, having four strain gauges mounted in precise locations on the structure. The strain gauges form a full Wheatstone bridge in a special arrangement: without externally applied force the bridge is balanced, when the two opposite positioned gauges are in compression, the other two will be in tension, thus the unwanted influences of the temperature and thermal expansion are eliminated. The load cells are active transducers, they need a supply voltage to work properly. One of the most common shape for a load cell is the double bending sheer beam (Fig. 3 a and b) [19, 20].
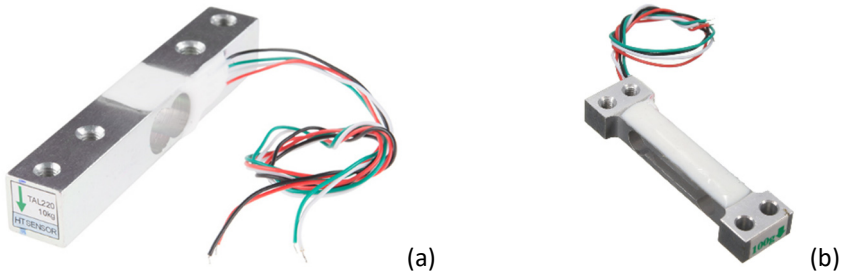
Fig. 3 Load cells: (a) beam (max. 10 kg), (b) mini (max. 100 g)

Although the electrical signal output is directly proportional to the product between the supply voltage and the relative change in resistance, it is still very small and requires specialized amplification and analog-to-digital conversion (Fig. 4) in order to be used in measurement systems based on computer or microcontrollers [21].
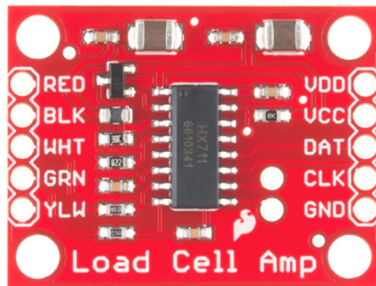
Fig. 4 The HX711 load cell amplifier

STIFFNESS TESTER DESIGN AND IMPLEMENTATION

Besides reliability, low-cost and the stand-alone status were the most important requirement for the bending stiffness tester designed and implemented as graduation thesis. Keeping in sight the values of bending stiffnesses for common papers and paperboards, a 100 g mini load cell and the two-point method were selected.

The schematic of the electronic circuitry (wiring, device driving, data acquisition, processing and display) is presented in Fig. 5 [22].
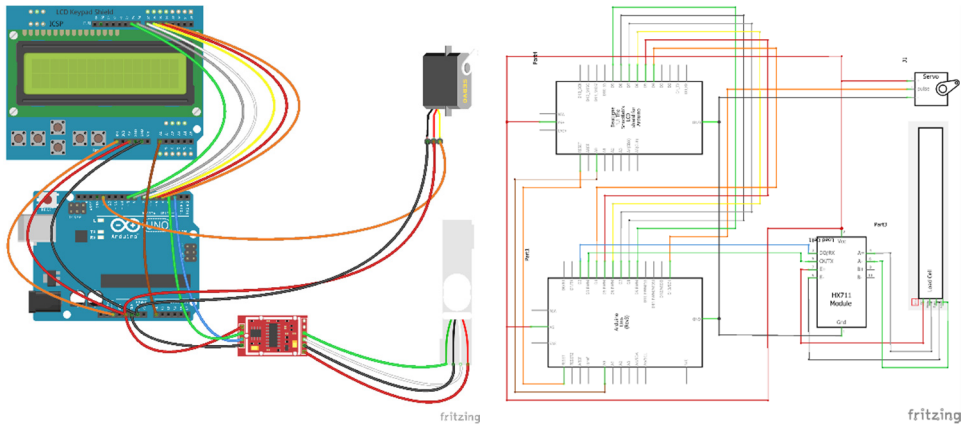
Fig. 5 Electronic circuitry

For driving, data acquisition and processing an Arduino Uno [23] microcontroller was selected. It drives the HX711 load cell amplifier and the Tower Pro MG90S type micro servo motor [24], which is used in the bending process of the paper samples. A LCD-S-1602-BLUE type display [25] was used to ensure that the measurement results can be displayed computer independently. The mechanical design was performed using Autodesk Inventor Professional software package [26]. The tester has only one moving component, the deflector disk which ensures the bending. It was made out from brass using CNC machining technology (Lang Impala 200LNC). All other pieces were obtained via PLA based 3D printing technology (DIY Cartesian FDM). As regarded the rectangular paper test piece, it was dimensioned according to the TAPPI T 489 om-08 standard [27]: 38.1 ± 0.3 mm in width and 70 ± 1 mm in length. This piece is immobilized in the sample holder at one of its free ends. At 50 mm from this point, the deflector will ensure a 15° deflection in both directions. The force is measured by the load cell, the bending moment is calculated in both directions (force arm is 50 mm), the average is displayed in mNm units. The ready to use stiffness tester, with its most important parts, is presented in Fig. 6.
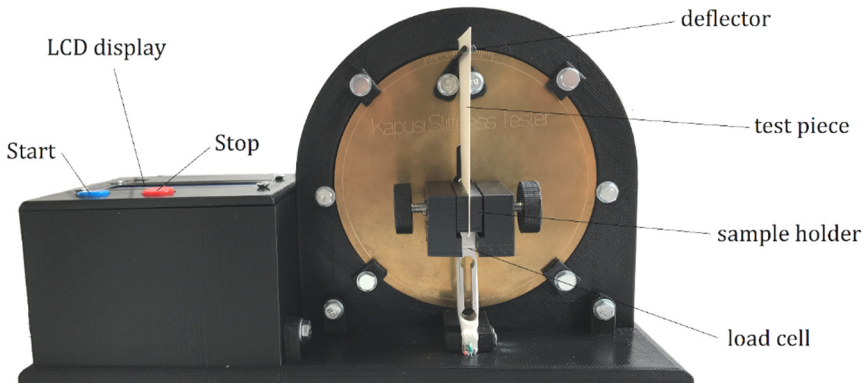
Fig. 6 The assembled bending stiffness tester assembled

CALIBRATION

The bending stiffness tester was calibrated in order to be able to display the bending moment in mNm units.
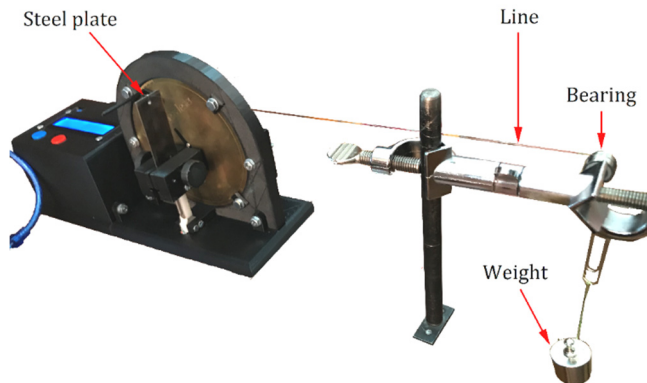
Fig. 7 Set-up for calibration

The calibration process is carried out by matching the measured force with a well-known value given by some analytical balance weights: a steel plate of the size of test pieces was inserted in the holder, the weights (0 g, 1 g, 2 g, 5 g, 10 g, 20 g, 50 g) were attached on it to ensure controlled value of force via line and bearing (Fig.7), bending moment was calculated by means of product between force and arm (l = 5 cm). The relationship between the measured load cell response and calculated bending moment is depicted in Fig.8. One can observe that there is an almost perfect linearity (r^2 = 0.99992) between them, the equation of the fit being:
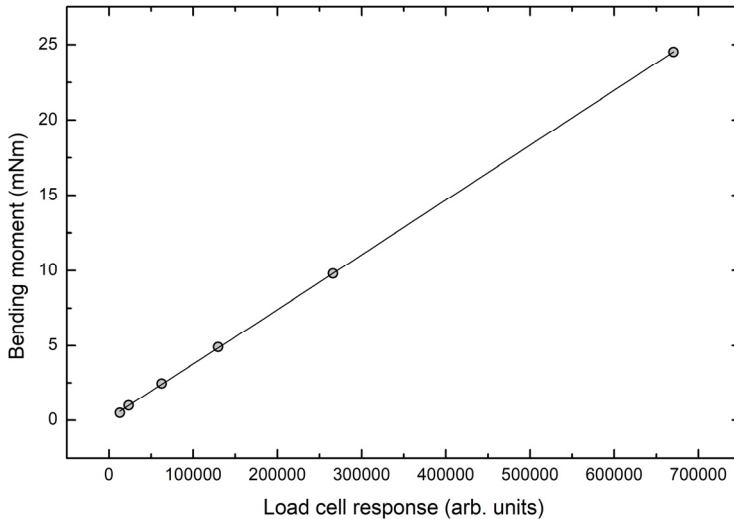
Fig. 8 Calibration curve

According to relationship (4), in the case of the two-point method, the bending stiffness is directly proportional to the bending moment. Subsequently, the Arduino code was implemented accordingly to this linear relationship and in any further measuring situation, the bending stiffness is displayed directly (in mNm units) on the LCD of the tester.

EXPERIMENTAL DETERMINATIONS

The reliability of the system was tested using some fully coated bleached paperboard with white back from Carta Solida [28]. The bending stiffnesses given by the manufacturer and those measured with our tester are presented and compared in Table 1.

As one can see the measured bending stiffnesses are in good agreement with the data given by vendor, the maximum relative error being around 7 %. Experimentally determined data have lower values due to different environmental testing conditions (temperature, humidity), but are well within the tolerance given by vendor (Fig. 9). Tests were performed also on some common, everyday life, commercially available products (Fig. 10), too.
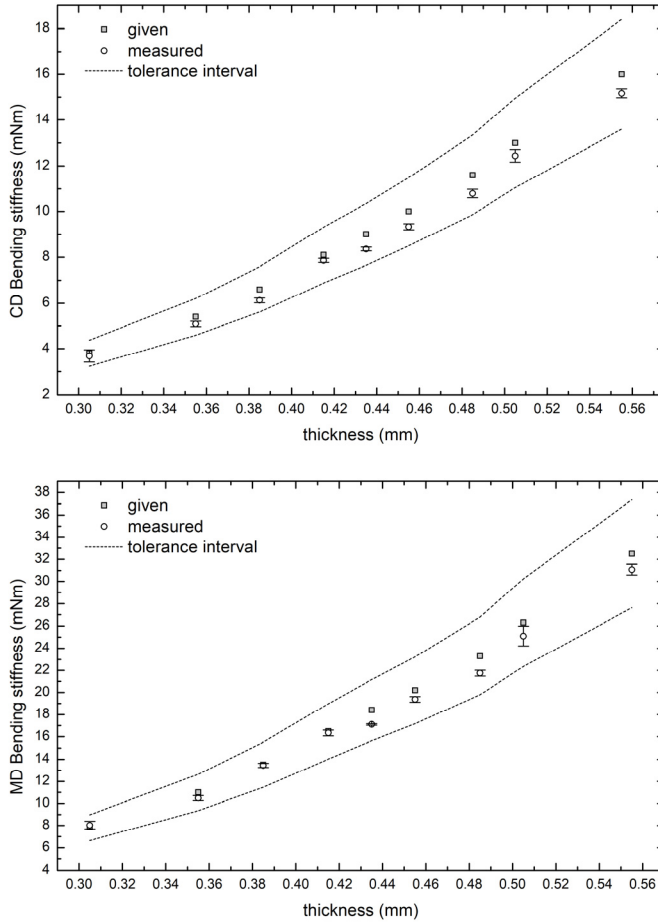
Fig. 9 Comparison between experimentally determined bending stiffnesses and vendors data as function of thickness and machine direction

milk box   pasta box   gift bag   ID badge paper   water PET

Fig. 10 Common tested products

Table 1. Bending stiffness measurements
on certified Carta Solida products

Grammage / Thickness / Orientation [1]			Bending stiffness (mN·m)		RE [4]
			Given [2]	Experimental [3]	
200	0.305	CD	3.80	3.684 / 0.266	- 3.16
200	0.305	MD	7.80	8.034 / 0.357	+ 2.95
225	0.355	CD	5.40	5.088 / 0.119	- 5.74
225	0.355	MD	11.00	10.485 / 0.237	- 4.64
235	0.385	CD	6.60	6.13 / 0.105	- 7.12
235	0.385	MD	13.50	13.446 / 0.190	- 0.37
250	0.415	CD	8.10	7.863 / 0.092	- 2.96
250	0.415	MD	16.50	16.337 / 0.260	- 0.97
260	0.435	CD	9.00	8.355 / 0.080	- 7.11
260	0.435	MD	18.40	17.108 / 0.063	- 7.01
270	0.455	CD	10.00	9.33 / 0.134	- 6.70
270	0.455	MD	20.20	19.373 / 0.266	- 4.11
285	0.485	CD	11.60	10.793 / 0.190	- 6.98
285	0.485	MD	23.30	21.749 / 0.276	- 6.65
295	0.505	CD	13.00	12.436 / 0.274	- 4.31
|295	0.505	MD	26.30	25.094 / 0.883	- 4.60
320	0.555	CD	16.00	15.168 / 0.195	- 5.19
320	0.555	MD	32.50	31.068 / 0.498	- 4.40

[1] Grammage in g/m^2, Thickness in mm, Orientation: CD cross machine / MD machine;
[2] Testing method: Taber 15 (ISO 2493), Tolerance: ± 15 %; [3] Average / Standard deviation
of 10 measurements; [4] Relative error in % (Given – Experimental)/ Given

The test pieces for the common materials were prepared and the measurements were performed according to the methodology described above. The results are presented in Table 2.

Table 2. Bending stiffness measurements on common products

Product	Fiber orientation	Bending stiffness (mN·m) *
pasta box	CD	10.31 / 0.10
	MD	23.21 / 0.11
milk box	CD	9.23 / 0.11
	MD	18.90 / 0.14
wine gift bag	CD	14.74 / 0.12
	MD	28.57 / 0.16
ID badge paper	CD	2.09 / 0.02
	MD	2.93 / 0.02
PET	none	6.80 / 0.04

* Average / Standard deviation of ten measurements

CONCLUSIONS

We have proposed a low-cost bending stiffness tester as a graduation project for Engineering Physics. The student designed and implemented a microcontroller driven device, the over-cost being around 100 EURO. The device was calibrated and measurements were performed on both commercially available certified paper products and some everyday life paper-based products.

The results obtained are in good agreement with literature. The project was an important diagnostic tool for the students' performances and skills, and it was successfully presented at the final graduation exam.

REFERENCES

1. Z. Kapusi, "Measurement of some mechanical properties of fibrous materials" BSc Thesis, Engineering Physics, Faculty of Physics, Babes-Bolyai University, Romania, July 2019.
2. H. Holik, "Handbook of Paper and Board" 1st ed. Weinheim: WILEY-VCH Verlag GmbH & Co. KGaA, 2006
3. M. J. Kirwan "Handbook of Paper and Paperboard Packaging Technology" 2nd ed. London: Wiley-Blackwell, 2013
4. M. Ek, G. Gellerstedt and G. Henriksson, "Pulp and Paper Chemistry and Technology Vol. 4 - Paper Products Physics and Technology" 1st ed. Berlin: Walter de Gruyter GmbH & Co. KG, 2009
5. ISO 5628:1990. Paper and board - Determination of bending stiffness by static methods - General principles

6. SCAN-P 65:91. SCAN-Test Method SCAN-P 65:91, Corrugated fibreboards and boards - Bending stiffness -Four-point method
7. ISO 5628:2012. Paper and board - Determination of bending stiffness - General principles for two-point, three-point and four-point methods
8. ISO 5629:2017. Paper and board - Determination of bending stiffness - Resonance method
9. Thwing-Albert Instrument Company, USA. The Stiffness Tester 150-E Brochure
10. Testing Machines Incorporated, USA. The Bending Resistance Tester Model 79-25 Brochure
11. Corporate Consulting, Service & Instruments, Incorporated, USA. Taber Model 150-E Digital Stiffness Tester Brochure
12. Corporate Consulting, Service & Instruments, Incorporated, USA. Stiffness Tester 150-E Brochure
13. ABB AB / Lorentzen & Wettre, Sweden. L&W Bending Tester Brochure
14. Haida International Equipment Ltd, Hong Kong. Four Point Bending Stiffness Tester Brochure
15. National Instruments White Paper - Measuring Strain with Strain Gages
16. W. Thomson, *Philosophical Transactions of the Royal Society*, 146/I, 730–736. (1856)
17. E. E. Simmons, Material Testing Apparatus, U.S. Patent No. 2292549 (1942).
18. A. C. Ruge, Strain Gauge, US-Patent No. 2350972 (1944)
19. SparkFun - Load Cell - 10kg, Straight Bar (TAL220) datasheet
20. SparkFun - Mini Load Cell - 100g, Straight Bar (TAL221) datasheet
21. SparkFun - Load Cell Amplifier - HX711 datasheet
22. Fritzing – Electronics made easy, http://fritzing.org/home/ (accessed 08.12.2018)
23. Arduino Uno, https://store.arduino.cc/arduino-uno-rev3 (accessed 02.11.2018)
24. MG90S digital servo datasheet
25. 1602 Blue LCD module HD44780 16x2 datasheet
26. Autodesk® Inventor® software, https://www.autodesk.com/education/free-software/inventor-professional (accessed 08.12.2018)
27. T 489 om-08 test method. Bending Resistance (Stiffness) Of Paper and Paperboard (Tabertype Tester In Basic Configuration)
28. Carta Solida Product Sheet

IN VIVO ^{1}H NMR RELAXOMETRY MAPS OF WOMEN NORMAL AND CANCEROUS PELVIS

I. A. MORAR[1,2], R. PINTICAN[3], R. E. DAVID[2],
T. KOVACS[2] and R. FECHETE[1,4*]

ABSTRACT. Transverse relaxation time (T_2) and ^{1}H spin density (ρ_{1_H}) parameter maps were obtained for the pelvis of two women. For that, two anatomical magnetic resonance (MR) images were recorded in axial orientation with a low echo time (TE1 $\cong$ 30 ms) and a large echo time (TE $\cong$ 200 ms) for a volunteer with normal pelvis and a patient with endometrial cancer. The largest T_2^{av}–value was obtained for the right pelvic bones of patient with endometrial cancer and the lowest one was obtained for the uterus of volunteer with normal pelvis.

Keywords: In vivo ^{1}H NMR imaging, T_2 and ρ_{1_H} parameter maps, axial normal pelvis images, axial pelvis with endometrial cancer, T_2^{av}–values of woman pelvis components.

INTRODUCTION

The pelvis is the lower part of the trunk of the human body. It is situated between the abdomen and the thighs. Together with the lower limbs sustains the entire weight of the upper body and have an essential role on the body posture, stability and balance [1]. The pelvic region is delineated by the pelvic bones and divided in pelvic cavity, pelvic floor and perineum. The pelvic skeleton is formed posteriorly by the sacrum and the coccyx and anteriorly by left and right hip bones. The pelvis anatomy varies between male and female. The female pelvis is wider and lower than de male pelvis and includes the uterus with its endometrium, myometrium and serous layers.

[1] Babeş-Bolyai University, Faculty of Physics, 1 Kogălniceanu str., 400084 Cluj-Napoca, Romania

[2] IMOGEN, County Emergency Hospital, Cluj-Napoca, Romania

[3] Iuliu Hatieganu University of Medicine and Pharmacy, Department of Radiology, Cluj-Napoca, Romania

[4] Technical University of Cluj-Napoca, Faculty of Material and Environmental Engineering, B-dul Muncii 103-105, Cluj-Napoca, Romania

[*] Corresponding author: rfechete@phys.utcluj.ro

The cells in human bodies have a certain role. The normal ones divide in an orderly way. Then they die when they are worn out or damaged, and new cells take their place. Cancer is a cureless disease caused by the "out of control cells" growth. The cancer cells keep on growing and dividing into new cells which crowd out normal cells. This means that old or damaged cells survive when they should die, and new cells form when they are not needed. These extra cells can divide without stopping and may form growths called tumors. There are many types of cancer in the pelvic area. One of the most frequent malignancies diagnosed in women is the uterine cancer [2].

Nuclear magnetic resonance (NMR) is a powerful technique used to investigate the living tissues by particular methods like magnetic resonance imaging [2, 3], ordered tissues [4] but also for imaging of materials [5]. Nevertheless, this can be successfully used in many areas. Recently, ^{1}H NMR relaxometry was used, for example, for assessing the wastewater treatment via the distributions of transverse relaxation time distributions [6].

The medical magnetic resonance imaging (MRI) is based on the phenomenon of nuclear magnetic resonance involving radiofrequency pulses applied to the human body being into a static magnetic field and appropriate magnetic field gradients for producing images with excellent soft tissue contrast [7]. To identify pathological anatomy it is necessary to obtain sufficient signal contrast between pathological and healthy tissue and sufficient spatial resolution to resolve small structures [8].

In everyday practice, radiological diagnosis is mainly based on the various magnetic resonance images weighted by relevant NMR parameters. A weighted image does not mean that it is influenced exclusively by that parameter [2]. To obtain for example transverse, T_2^*, longitudinal T_1^* or residual dipolar coupling parameter maps, simpler approaches are based on only two MR images [2, 4, 5, 9].

The aim of this paper is to obtain transverse relaxation time T_2 and ^{1}H spin density ρ_{1_H} parameter maps and to compare the specific values (minimum, maximum and the average) obtained for women's normal and cancerous pelvis. Statistical distributions of T_2 and ^{1}H spin density for four pelvic areas such as uterus, bone, fat and muscles are evaluated.

EXPERIMENTAL

Patients

Prior to the start of the clinical investigations, a written informed consent was obtained from all volunteers. Two female patients were enrolled in this study, one with normal endometrium (age 46) and the other with endometrial cancer (age 72).

The first one has an regulate menstruation and the other is at menopause. Both of them had 2 previous gestations (caesarian section) and underwent gynecological examinations (Papanicolaou test [10]) and pelvic ultrasonography.

Methods

The volunteer and the patient were investigated on a GE 3T MRI Discovery MR750w. The average total scanning time was 1 hour. A body coil transmission with 16-channel phased-array receiver was used. 10 Minutes before starting the MRI investigation, an antispasmodic drug was administrated intravenously to reduce movement artifacts. Additional to axial T2 Spin Echo FRFSE-XL pulse sequence used for obtaining the T_2^* and ρ_{1_H} parameter maps, the protocol include at the beginning a localization pulse sequence and a diffusion weighted imaging sequence at the final of investigation. Two acquisitions were obtained with the same repetition time (TR – recycle delay) 5000 ms but different echo times TE_1 = 30 ms and TE_2 = 200 ms. The section thickness was 4 mm, the field of view (FOV) 350-400 mm, the intersection gap was 0.8 mm, matrix size (in frequency and in phase encoding) was 384x256.

RESULTS AND DISCUSSION

Figure 1 presents the anatomic MR images in axial orientation recorded for a normal woman pelvis (left images) and a woman pelvis with endometrial cancer with two values of echo time (TE) of 30 ms (top) and 200 ms (bottom). Some major anatomic components that can be distinguished are: i) the uterus (located in the center-top of approximately circular shape and a neutral gray color); ii) The bladder observed only for the woman with cancer on top of uterus (see Figs. 1 c) and d)); iii) sections in the left and right innominate bones (as a thin formation with diagonal orientation starting from top left and right toward bottom center of open gray color surrounded by a darker color); iv) muscles: puborectalis, pubococcigeus, ilicoccygeus, ischiococcygeus, obturator internus and piriformis (having a darker color); v) fat (lipid cells) surrounding the body's internal organs observed with the lighter color and vi) rectum (with darker color in centrum). One can remark that existence of cancerous cells the uterus is deformed (see Figs. 1 c) and d)).

In order to obtain the T_2 parameter map ($T_2^{(x,y)}$), one have to calculate voxel by voxel (for all *x* and *y* coordinates) the ratio between the upper MR image in Fig. 1 expressed as an $S_1^{(x,y)}$ matrix characterized by
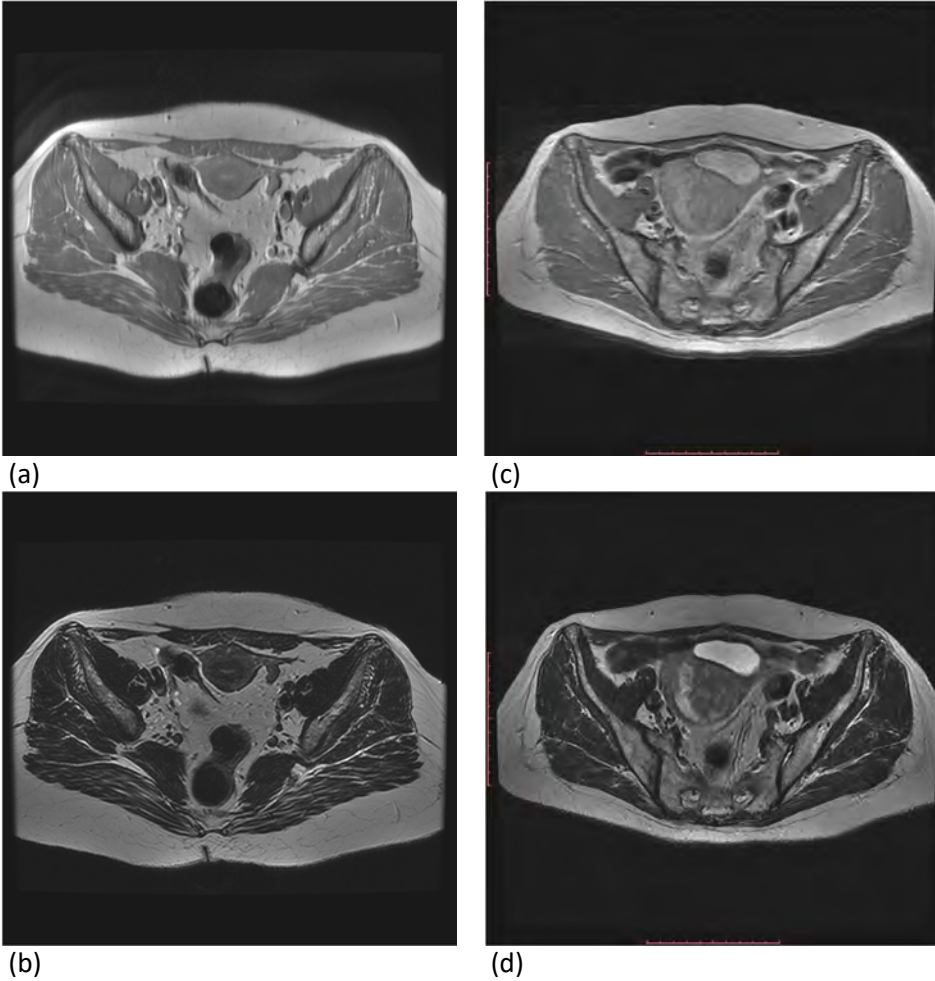
Fig. 1 Axial T2 weighted MR images of a volunteer woman (left) recorded with (a) TE = 30 ms and (b) TE = 200 ms and a patient woman with endometrial cancer (right) recorded with (c) TE = 30 ms and (d) TE = 200 ms.

the low echo time (TE$_1 \cong 30$ ms in our case) and the lower MR image expressed as an $S_2^{(x,y)}$ matrix characterized by the high echo time (TE$_2 \cong 200$ ms in our case) as [2],

$$T_2^{(x,y)} = \frac{TE_2 - TE_1}{ln\left[\frac{S_1^{(x,y)}}{S_2^{(x,y)}}\right]}.$$

(1)
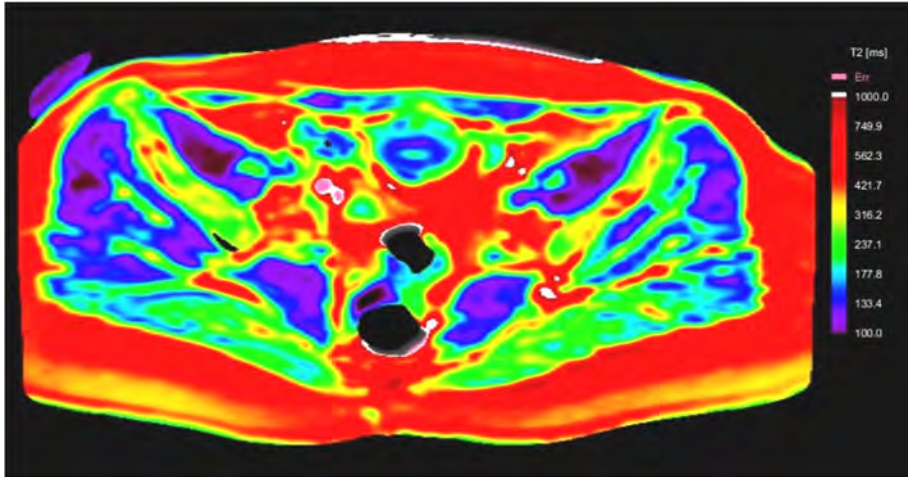
(a)
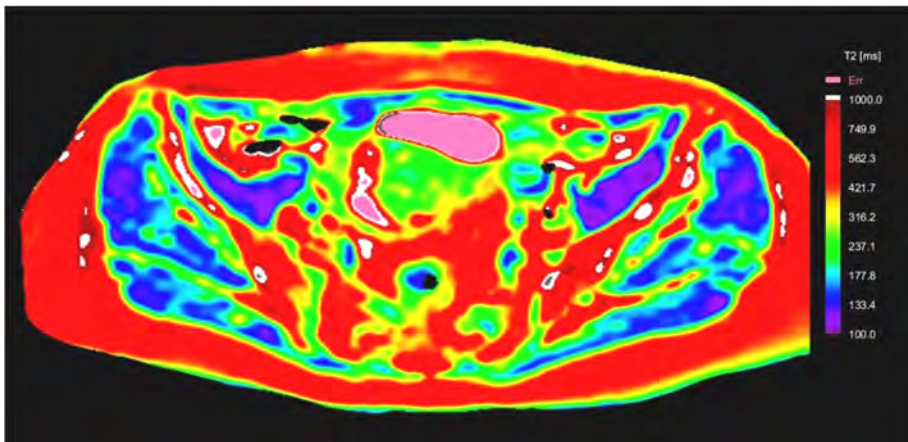
(b)

Fig. 2 The T_2 maps obtained using eq. (1) from images presented in Figs. 1 for
a) normal pelvis and b) endometrial cancer.

The T_2 parametric maps calculated using eq. (1) from T2 weighted MR images for the normal and affected by endometrial cancer with myometrial invasion are presented in Fig. 2. Compared with the T_2 parameter maps reported in

[9] obtained for a three tube phantom, the contrast and resolution of our map are net superior. The limits for T_2-values were set to 100 ms for the minimum value and 1000 ms for the maximum value. A T_2-value larger than 1 s is represented with white color, while a T_2-value smaller than 100 ms is represented with black color. The fat cells present large T_2-values and are observed as extended red regions. The muscular formations presents the smallest T_2-values and are observed as regions colored in violet, blue up to green colors (for the patient with cancer), meaning that the specific T_2-values are in the range of 100 ms up to 180 ms and containing the green for the normal patient with the T_2-values in the range of 100 ms up to 300 ms. The bones being a porous/spongy biomaterial is characterized also by large T_2-values. Differences can be observed between the volunteer and patient, meaning that the volunteer with normal uterus present lower T_2-values (see Fig. 2a) compared to the patient with endometrial cancer (see Fig. 2b). The uterus of the volunteer with normal pelvis presents lower T_2-values than the values measured for the volunteer with endometrial cancer. This malign formation can be observed as the green area surrounding a red colored region characterized by high T_2-values.

Additional to the T_2 parameter map, for a radiologist, which usually establishes a diagnostic only from anatomic images (gray MRI presented in Fig. 1) significant information can be obtained from ρ_{1_H} parameter maps. In order to obtain the ρ_{1_H} parameter map one can use the previously calculated T_2^* parameter map. The specific equation for a ρ_{1_H} parameter map is given by [2],

$$\rho_{1_H}^{(x,y)} = S_i^{(x,y)} \cdot e^{+\frac{TE_i}{T_2^{(x,y)}}}, \tag{2}$$

where $S_i^{(x,y)}$ can be the map S_1 corresponding to the short echo time or the second map S_2 recorded with long echo time. Due to the large signal to noise ratio (SNR), we used the MR image recorded with a short echo time. The ρ_{1_H} parameter maps obtained for our women are presented in Figs. 3.

(a)

(b)
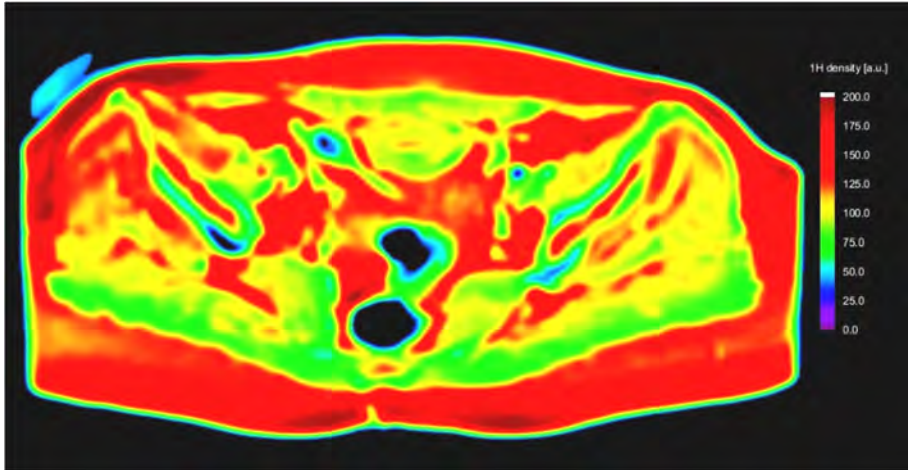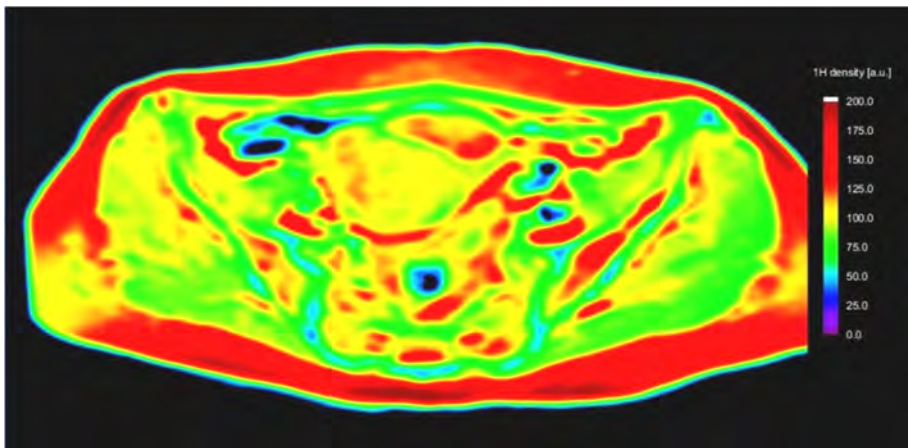
Fig. 3 The ρ_{1_H} parameter maps obtained using eq. (2) from images presented in Figs. 1 for a) normal pelvis and b) endometrial cancer

The areas with a small number of protons are represented in blue and are mainly observed around the rectum and large bowel section. The areas with a large number of protons are represented in dark red and are found in lateral front and middle back fat regions. A large number of protons (red) can be found in fat that surround the internal organs. In yellow and green are represented the organs with intermediate number of protons.

(a)

(b)

(c)

(d)

(e)

(f)
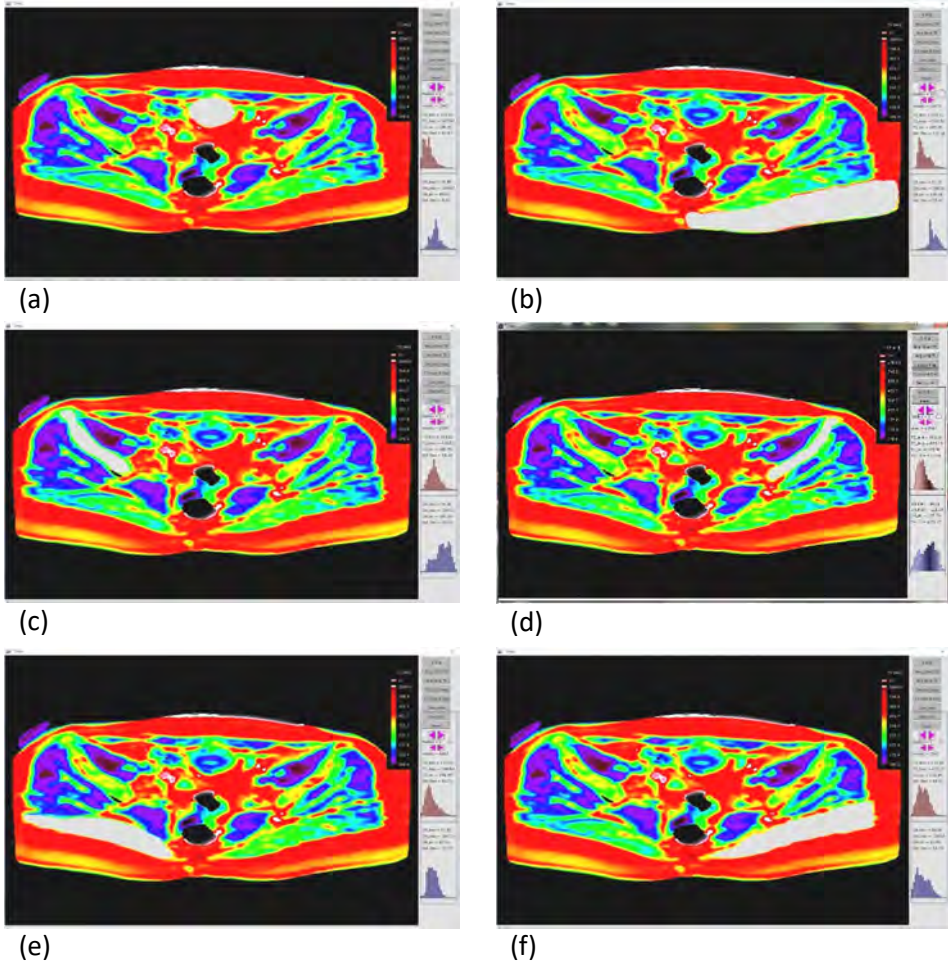
Fig. 4 Statistical distributions of minimum, maximum and average values of T_2 and ρ_{1_H} parameter for various ROIs of a normal pelvis (a) uterus; (b) fat; (c) left innominate bone; (d) right pelvic bones; (e) left piriformis muscle and (f) right piriformis muscle. The ROI is marked with gray color.

In Fig. 4 are represented (as a screen capture of our processing software) the statistical distributions of minimum, maximum and average values of T_2 and ρ_{1_H} parameters for various regions of interest (ROIs) marked with gray color for a normal pelvis. These are the uterus (Fig. 4a), fat (Fig. 4b), left innominate bone (Fig. 4c), right pelvic bones (Fig. 4d), left piriformis muscle (Fig. 4e) and right piriformis muscle (Fig. 4f).
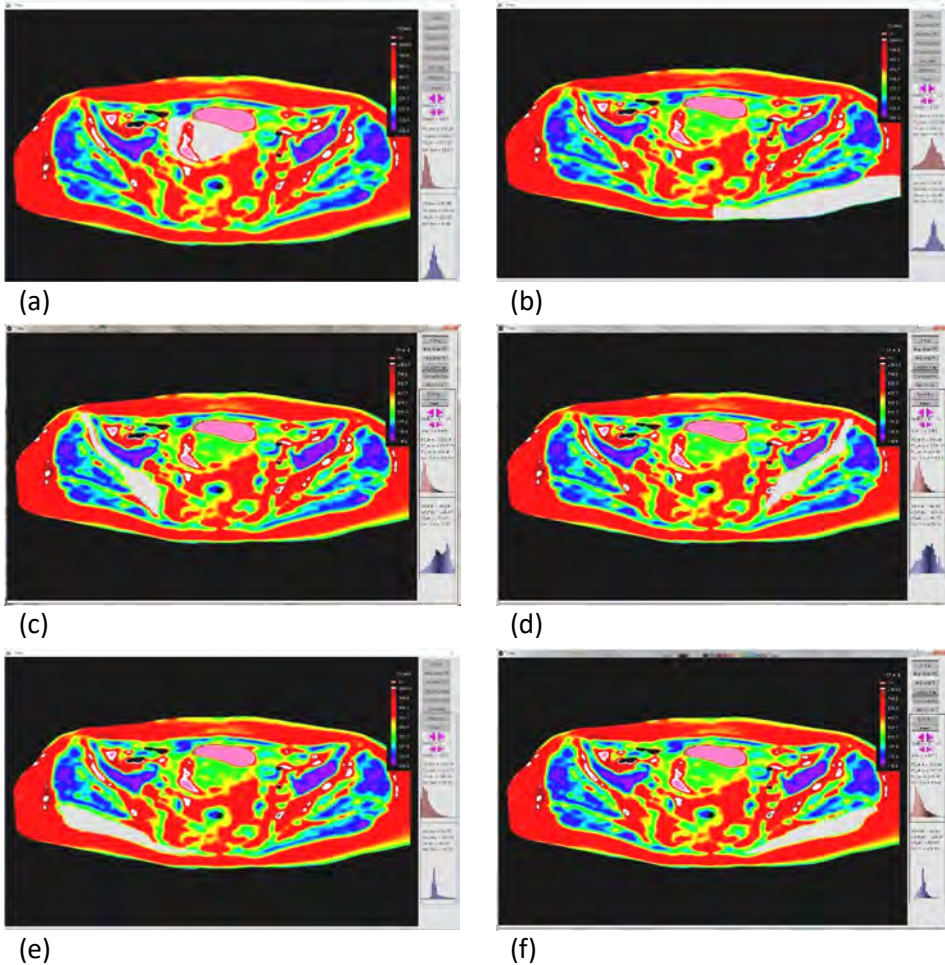
Fig. 5 Statistical distributions of minimum, maximum and average values of T_2 and ρ_{1_H} parameter for various ROIs of a pelvis with endometrial cancer (a) uterus; (b) fat; (c) left pelvic bone; (d) right pelvic bones; (e) left piriformis muscle and (f) right piriformis muscle. The ROI is marked with gray color.

The statistical distributions of minimum, maximum and average values of T_2 and ρ_{1_H} parameter of a pelvis with endometrial cancer are shown in Fig. 5 for the same types of ROIs as in the case of normal pelvis. The measured values are comparatively presented in Table 1 for the normal pelvis and in Table 2 for the pelvis with endometrial cancer. The statistical values are well defines, since the number of voxels are between 2042 for right bone and 13573 for fat both belonging to woman with normal pelvis. For this woman the lowest T_2^{av}-value was measured

Table 1. Minimum, maximum and average values of transverse relaxation times T_2 obtained for various ROI's as: uterus, fat, innominate bone or muscle.

ROI	Normal			Endometrial Cancer		
	T_2^{min} [ms]	T_2^{max} [ms]	T_2^{av} [ms]	T_2^{min} [ms]	T_2^{max} [ms]	T_2^{av} [ms]
uterus	122.6	403.0	186.4	175.3	682.2	273.6
fat	242.7	910.9	487.3	175.3	677.0	459.1
bone left	184.8	478.6	300.8	220.4	1919.8	586.3
bone right	159.6	625.2	329.1	164.4	1769.1	643.3
muscle left	137.5	398.7	218.4	125.8	424.7	186.5
muscle right	115.3	419.2	218.8	112.8	321.9	176.0

Table 2. Minimum, maximum and average values of proton spin density ρ_{1_H} obtained for various ROI's in the pelvis region.

ROI	Normal			Endometrial Cancer		
	$\rho_{1_H}^{min}$	$\rho_{1_H}^{max}$	$\rho_{1_H}^{av}$	$\rho_{1_H}^{min}$	$\rho_{1_H}^{max}$	$\rho_{1_H}^{av}$
uterus	76.9	129.7	99.2	80.9	137.4	102.6
fat	35.1	206.8	140.3	39.2	212.8	141.5
bone left	34.4	154.5	105.8	44.6	130.0	95.4
bone right	60.6	153.7	107.7	42.1	165.1	104.8
muscle left	57.8	144.1	87.3	50.7	151.4	93.6
muscle right	68.5	138.7	91.5	53.2	129.2	82.0

for uterus (186.4 ms), while the largest one was found for fat (487.3). In the case of woman with uterine cancer lower T_2^{av}-value were measured for muscle (186.5 ms and 176.0 ms) while the largest one was found not for fat (459.1 ms) but for innominate (hip) bone (586.3 ms and 643.3 ms). For this woman one can remark an increased T_2^{av} for uterus and bone. As expected the largest $\rho_{1_H}^{av}$– values were measured for fat tissue and the smallest one was measured for muscle, then for uterus and bone. Form $\rho_{1_H}^{av}$ no significant differences between normal and cancerous pelvis are observed.

CONCLUSIONS

T_2 and ρ_{1_H} parameter maps were obtained for the pelvis of two women, a volunteer with normal pelvis and a patient with endometrial cancer. The statistical T_2^{av} and $\rho_{1_H}^{av}$– values calculated from these maps on various pelvic components

such as uterus, fat, bone or muscle show significant differences between normal pelvis compared to the pelvis with endometrial cancer. Abnormalities of T_2^{av}-values are also observed in the case of patient with the endometrial cancer like large T_2^{av} for uterus.

REFERENCES

1. P. Abrahams (Editor), How the body works, Ed. Amber Books Ltd., London 2016
2. R. E. Dávid, R. Fechete, S. Sfrângeu, D. Moldovan, R. I. Chelcea, I. A. Morar, F. Stamatian, T. Kovacs, P. Popoi, *Anal. Lett.*, 52(1) 54-77 (2019)
3. E. Epstein, and L. Blomqvist, *Best Practice & Research Clinical Obstetrics & Gynaecology,* 28 (5) 721–39 (2014)
4. R. Fechete, D. E. Demco, and B. Blümich, *J. Magn. Reson.,* 165, 9–17 (2003)
5. D. Demco, A.-M. Oros-Peusquens, L. Utiu, R. Fechete, B. Blümich, N. J. Shah, *J. Magn. Reson.,* 227, 1–8 (2013)
6. R. Crainic, L. R. Drăgan, R. Fechete, STUDIA UBB Physica, 63 (1-2) 49-60 (2018)
7. S. Clare, Functional Magnetic Resonance Imaging: Methods and Applications, Nottingham (1997)
8. R. Buxton, Introduction to Functional Magnetic Resonance Imaging, 2nd edition, Cambridge University Press, Cambridge (2009)
9. L. Fanea, S. A. Sfrangeu, *Romanian Rep. Phys.*, 63(2) 456-64 (2011)
10. L.G. Koss, *J. American Med. Ass.,* 261(5):737-43 (1989)

SCREENING OF POTENTIAL NEW SOLID FORMS OF VITAMIN B1 WITH VITAMIN B3

M. MURESAN-POP[1], D. M. PETRISOR[1*], S. SIMON[1,2]

ABSTRACT. The present study aimed to obtain new solid forms between Vitamin B1 (thiamine hydrochloride) and Vitamin B3 (nicotinamide) following the mechanochemistry route. The samples prepared by grinding in different solvents, of thiamine hydrochloride with nicotinamide in 1:1 and 1:2 molar ratios were investigated by X-ray diffraction (XRD) and Fourier transform infrared spectroscopy (FTIR). The XRD and FTIR results point out that for the chosen ratios of components and for the aqueous ethanol solution and for ethyl acetate used as solvents, none solid forms were obtained, but only physical mixtures. For the sample with 1:2 molar ratio of B1:B3, the FTIR analysis reveals very small changes of few absorption bands consisting in a weak shift towards higher wavenumbers, due to grinding process.

Keywords: thiamine hydrocloride; nicotinamide; mechanochemistry; XRD; FTIR.

INTRODUCTION

Mechanochemistry is a method that uses mechanical force to initiate chemical reactions. A popular tool choice amongst mechanochemical researchers is the ball mill (BM), which also is used for forcing bulky molecules to react [1]. Solvent-drop grinding is an effective screening tool, that requires small amount of solvent, and gives often the possibility of create new co-crystals, which are not traditionally obtainable [2].

Solubility of pharmaceutical compounds is an important step in the development of the final product, and co-crystallization is one of the most common operations used to obtain new solid forms with improved properties.

[1] *Interdisciplinary Research Institute on Bio-Nano-Sciences, Babes-Bolyai University, 400271 Cluj-Napoca, Romania*

[2] *Faculty of Physics & Interdisciplinary Research Institute on Bio-Nano-Sciences, Babes-Bolyai University, 400084 Cluj-Napoca, Romania*

* Corresponding author: dinapetrisor@yahoo.co.uk

Thiamine hydrochloride belongs to a class of water-soluble vitamins essential for the body and is also called Vitamin B1. It has the chemical structure $C_{12}H_{18}Cl_2N_4OS$ (Fig. 1a) and has the molar mass 337.3 g/mol. Thiamine hydrochloride is a hygroscopic salt. This compound plays an important role in the digestive system, nervous system and normal activity of the heart [3-5], and is mainly used in animal feed as nutritional supplements, as well as in the feed industry, in medicines, but also in cosmetic products [6,7]. Various new solid forms of thiamine hydrochloride have been reported in the literature [8,9]. It has been shown that hemihydrate form of thiamine hydrochloride is the most stable in contact with water up to 120ºC, when dehydration of the substance begins [8,10].
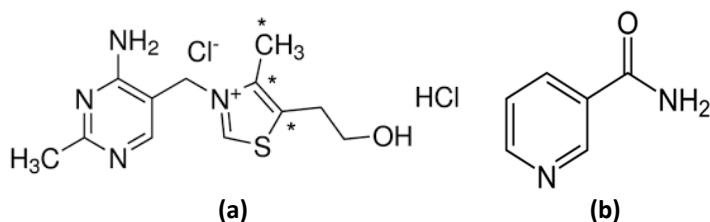
Fig. 1 Chemical structure of thiamine hydrochloride (a) and nicotinamide (b).

In the field of pharmaceutics, the new solid forms (solvates, hydrates, co-crystals and salts) play an important role in the design of new solid forms [11]. Differences in solid forms often lead to differences in thermodynamic parameters and physico-chemical properties (solubility, dissolution rate, stability and mechanical properties) [12].

The co-crystal formation involves the co-crystallization of an agent active pharmaceutical ingredient and another agent named coformer. Thus, the purpose of this study was to obtain new solid forms of thiamine hydrochloride, using nicotinamide as a coformer.

Nicotinamide ($C_6H_6N_2O$, Fig. 1b) is part of the class of vitamins B too, and is named vitamin B3. It is used as a dietary supplement and as a neuroprotective agent [13]. The molar mass of nicotinamide is 122.1 g/mol, about three times larger than that of nicotinamide. This was one of the reasons to consider nicotinamide as a possible conformer in obtaining new solid forms with thiamine hydrochloride, because in this case the forming of a complex seems to have a relative high probability. On the other hand, the nicotinamide molecule has donor sites, as pyridine ring nitrogen

(N+) and amino-nitrogen, while thiamine hydrochloride has 4 hydrogen bond acceptors, and 2 hydrogen bond donors. Therefore, the two molecules are expected to form new bonds.

In the present study were investigated two samples prepared by solvent assisted ball milling of vitamins B1 and B3, which were aimed to form by mechanochemistry solid forms of thiamine hydrochloride with nicotinamide as coformer. The samples were analyzed using X-ray diffraction and infrared spectroscopy.

EXPERIMENTAL

Thiamine hydrochloride (THC) and nicotinamide (NICA) provided by Alfa Aesar and Sigma Aldrich, respectively, were used without any further purification. Two samples with thiamine hydrochloride and nicotinamide were prepared as follows:

1. THCNICA-BM1: 25 mg THC (0.074 mmol), 9.14 mg NICA (0.074 mmol), were ground together for 60 minutes using a Retsch MM200 ball mill, with 40µl aqueous ethanol solution (EtOH / water, 1: 1 v / v)

2. THCNICA-BM2: 25 mg THC (0.074 mmol), 2x9.14 mg NICA (2x0.074 mmol), were ground together for 60 minutes using a Retsch MM200 ball mill, with 40µl ethylacetate.

After milling, the samples were dried at 37ºC before analysis by powder X-ray diffraction and infrared spectroscopy.

The structural analysis was made by X-ray powder diffraction using a Shimatzu XRD-6000 diffractometer with graphite monochromator. The measurements were performed at room temperature, in 2θ range between 3–40°, with Cu K_α radiation (λ = 1.5406 Å, operating conditions 40 kV and 30 mA).

For the analysis by Fourier-transform infrared spectroscopy (FTIR) 1.6 mg of each sample were well mixed with 150 mg KBr of spectroscopic grade purity, and pressed into 13 mm diameter disks under a pressure of 12 tons. The measurements were carried out with a JASCO 6200 FTIR spectrometer (256 scans; resolution 4 cm^{-1}; spectral range 4000-400 cm^{-1}) and the recorded spectra were analysed using Spectra Analysis software.

RESULTS AND DISCUSSION

The X-ray powder diffraction patterns obtained for solvent assisted ball milled THCNICA-BM1 and THCNICA-BM2 samples was compared with that of the starting thiamine hydrochloride (THC) and nicotinamide (NICA). From X-ray diffractograms (Fig. 2)

one observes that in both cases, after milling, all diffraction lines represent a superposition of the diffraction lines corresponding to the ball milled components. There are no new lines to signalize the achievement of a new structure and no lines from thiamine hydrochloride and nicotinamide patterns are missing.
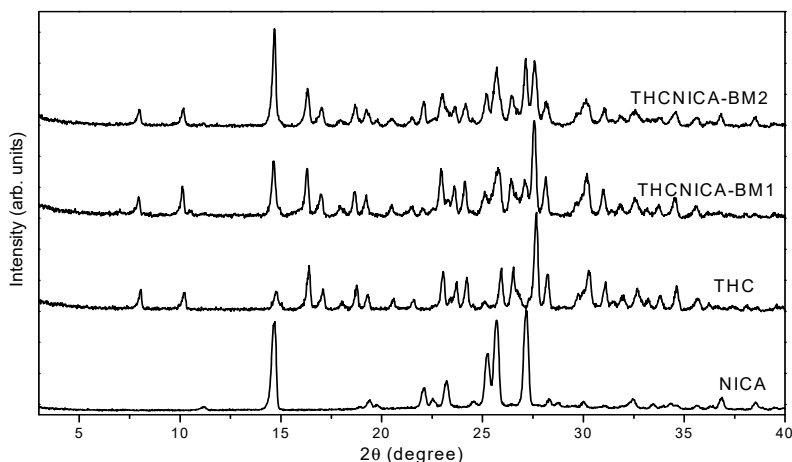

Fig. 2 X-ray powder diffraction patterns of thiamine hydrochloride and nicotinamide along with the powder diffraction patterns of the samples obtained by their solvent assisted ball milling.

Concerning the difference observed in the intensities of the diffraction lines recorded from the ball milled samples, this clearly reflects the double amount of nicotinamide used for BM-2 sample, wherein the ratio vitamin B1/vitamin B3 is half of the same ratio in BM-1 sample. According to these XRD results, no new solid forms of thiamine hydrochloride were developed, and only two physical mixtures were formed under the mentioned synthesis conditions.

Further analysis of the samples was carried out by Fourier transform infrared spectroscopy. The infrared spectra of starting materials THC and NICA (Fig. 3) were compared in the spectral range of interest with the spectra obtained for the solvent assisted ball milled samples THCNICA-BM1, THCNICA-BM2 (Fig. 4).

The FTIR spectrum of vitamin B1/ THC (Fig. 3a) contains characteristic bands of C-H stretching vibrations located at 3491 cm^{-1} and N-H stretch band at 3423 cm^{-1}; the N-H stretching vibrations at 3289 cm^{-1}, and C-N vibration at 3042 cm^{-1}; the N-H stretching vibration of primary amine is identified at 2909 cm^{-1}. The C-OH stretching vibration was observed at 1045 cm^{-1} and C-Cl at 766 cm^{-1} and 640 cm^{-1}.
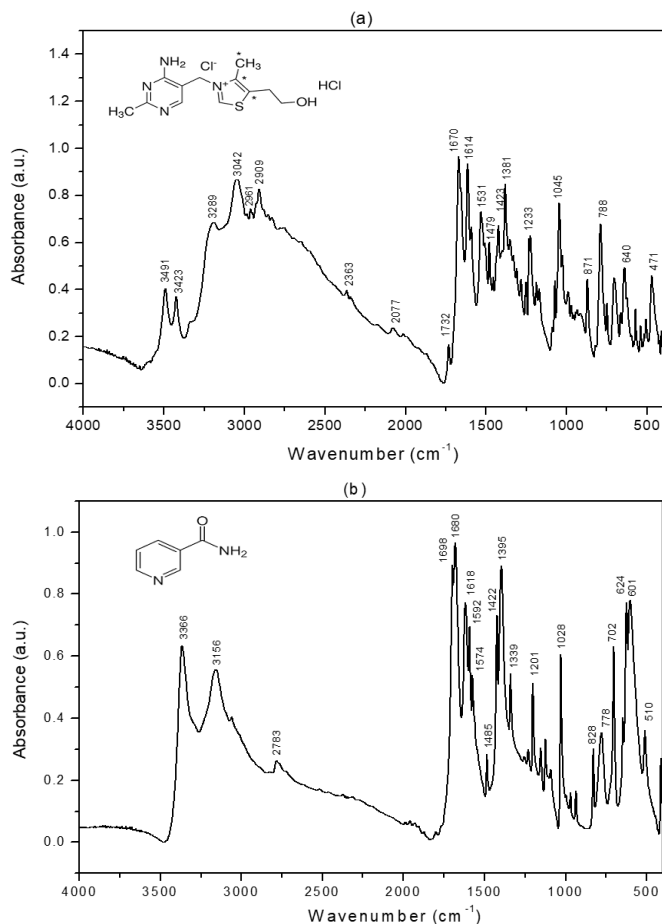
Fig. 3 FTIR spectra of thiamine hydrochloride (a) and nicotinamide (b).

In the FT-IR spectrum of Vitamin B3/NICA (Fig.3b) two strong characteristic bands appear at 3366 and 3156 cm^{-1}, attributed to asymmetric and symmetric stretching vibrations of the NH$_2$ group. Strong bands assigned to C=O bond vibrations are observed for nicotinamide at 1698 and 1680 cm^{-1} [14, 15]. The bands at 1614 cm^{-1} and 1618 cm^{-1} were attributed to NH$_2$ scissoring vibration [16].

By comparing the FTIR spectra of the obtained samples with the FTIR spectra of the starting materials (Fig. 4), it can observe that the characteristic bands of the starting materials are found in both prepared sample, without any major differences.
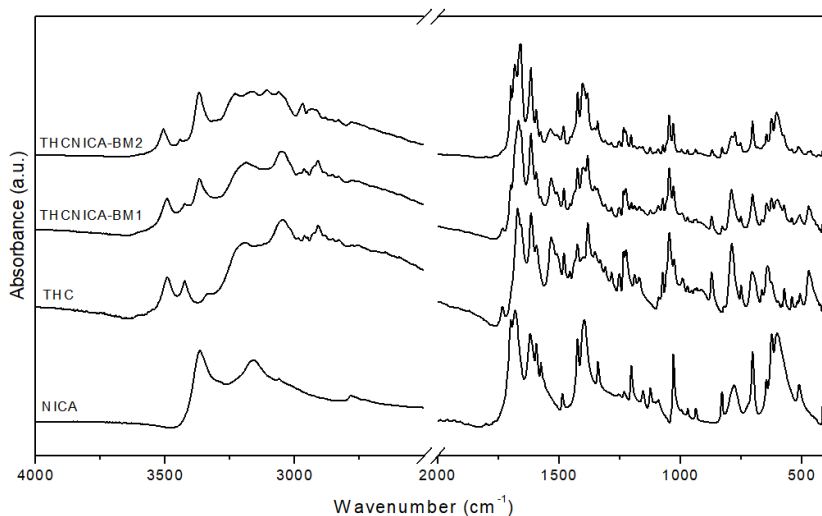
Fig. 4 FTIR spectra of nicotinamide (NICA) and thiamine hydrochloride (THC) along with the patterns of the samples obtained by their solvent assisted ball milling BM1 and BM2.

Further, if we compare the sum of the FTIR spectra for the starting materials (THC + NICA) with the FTIR spectra of the obtained samples, in the case of the THCNICA_BM1 sample, only a physical mixture between THC and NICA is highlighted (Fig. 5).
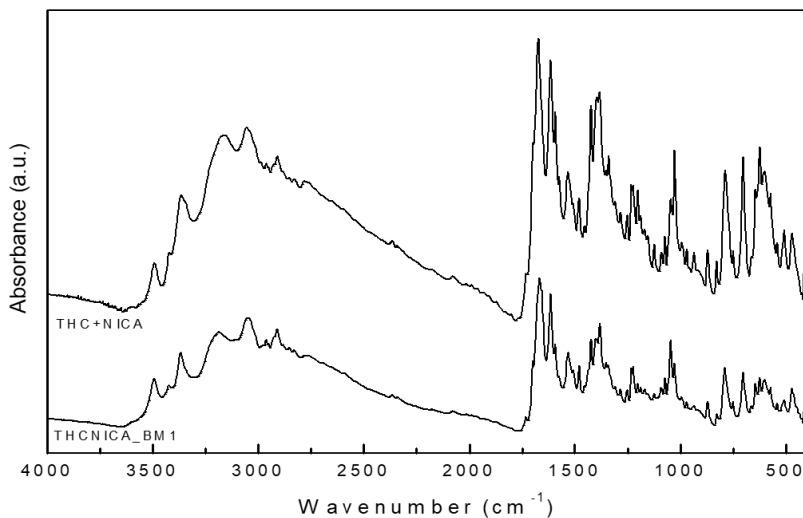
Fig. 5 Sum of FTIR spectra of thiamine hydrochloride and nicotinamide (THC+NICA) compared with the FTIR spectrum of the THCNICA_BM1 sample.

For the THCNICA_BM2 sample, it can be observed that a few absorption bands appear slightly shifted to higher wavenumbers, like the vibration from 3491 cm^{-1} who appears at 3506 cm^{-1}, and the one from 3423 cm^{-1} which appears at 3440 cm^{-1} (Fig. 6). It can be observed that these shifts are very small and cannot be attributed to the formation of new solid form of thiamine hydrochloride with nicotinamide as a coformer. Also, in the 3000 cm^{-1} ÷ 3300 cm^{-1} spectral region of FTIR spectrum of THCNICA_BM2 an overlapping bands can be observed, compared with the same region in the THC+NICA spectrum, where the same spectral lines are better resolved. This overlapping and the shifts too, are most likely due to the grinding process and the presence of water in the analyzed samples.
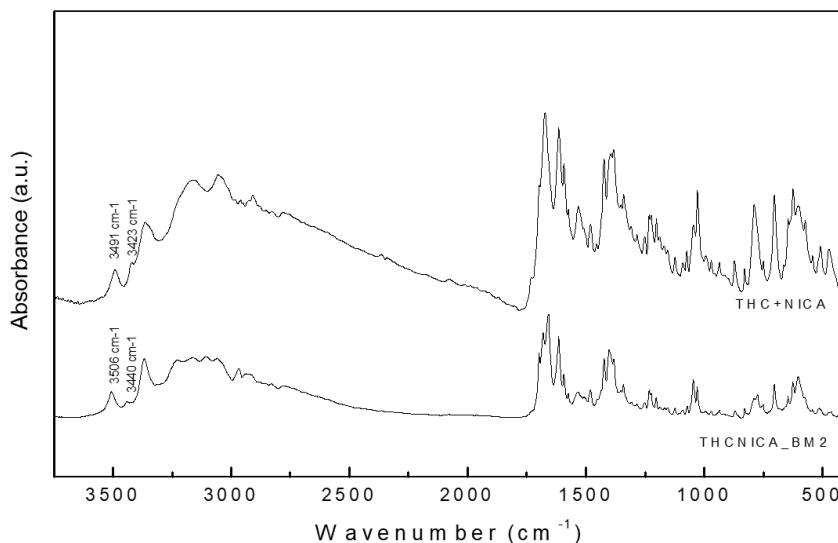
Fig. 6 Sum of FTIR spectra of thiamine hydrochloride and nicotinamide (THC+NICA) compared with the FTIR spectrum of the THCNICA_BM2 sample.

CONCLUSIONS

The present study aimed to obtain potential new solid forms by combining Vitamin B1 (thiamine hydrochloride) with Vitamin B3 (nicotinamide), in different molar ratios and using different solvents, by mechanochemistry method. Two physical mixtures were obtained using solvent drop grinding of thiamine with nicotinamide as coformer. For the THCNICA_BM2 sample the FTIR analysis reveals very small changes of few absorption bands, consisting in a weak shift towards higher wavenumbers and overlapping bands, due most likely to grinding process.

The results indicate that other molar ratios and/or other solvents should be investigated with regard to the use of Vitamin B3 as a conformer, or to consider other co-formers, in order to obtain new solid forms of Vitamin B1 with improved properties.

REFERENCES

1. J.L. Do & T. Frisčic, *ACS Central Science,* 3 (1), 13–19, (2016).
2. V. Andrew, D.A. Trask, W. D. Haynes, S. Motherwell & W. Jones, *The Royal Society of Chemistry, Chemical Communications,* 51–5, (2006).
3. D. J. Goldberg, T. B. Begenisich, & J. R. Cooper, *Journal of Neurobiology,* 6, 453–462, (1975).
4. B. Adamolekun, W. Adamolekun, A. D. Sonibare, & G. Sofowora, *Neurology* 44, 549–551, (1994).
5. K. D. Wrenn, F. Murphy, & C. M. Slovis, *Annals of Emergency Medicine,* 18, 867–70, (1989).
6. J. S. Hawker, C. F. Jenner, & C. M. Niemietz, *Australian Journal* of *Plant Physiology,* 18, 227–237, (1991).
7. A. Watanabe, S. Tasaki, Y. Wada, & H. Nakamachi, *Chemical and Pharmaceutical Bulletin* 27, 2751–2759, (1979).
8. P. Chakravarty, & R. Suryanarayanan, *Crystal Growth* & *Design* 10, 4414–4420, (2010)
9. P. Chakravarty, R. T. Berendt, E. J. Munson, V. G. Young, R. Govindarajan, & R. Suryanarayanan, *Journal of Pharmaceutical Sciences* 99, 816–827, (2010).
10. P. Chakravarty, R. T. Berendt, E. J. Munson, V. G. Young, R. Govindarajan, & R. Suryanarayanan, *Journal of Pharmaceutical Sciences* 99, 1882–1895, (2010).
11. C. Moisescu-Goia, M. Muresan-Pop, & V. Simon, *Journal of Molecular Structure* 1150, 37-43, (2017).
12. A.M. Healy, Z.A. Worku, D. Kumar, & A. M. Madi, *Advanced Drug Delivery Reviews* 117, 25–46, (2017).
13. R.A. Fricker, E.L Green, S.I Jenkins, & S.M Griffin, *International Journal of Tryptophan Research,* 11, 1–11, (2018).
14. A.S.H. Hameed & C.W. Lan, *Journal of Crystal Growth* 270, 475–480, (2004).
15. D. Kuaczkowska, A.L. Mazur, & W. Ferenc, *Journal of Thermal Analysis and Calorimetry,* 96 (1), 255–260, (2009).
16. S. Bayarı; A. Ataç; Ş. Yurdakul, *Journal of Molecular Structure* 655 (1), 163–170, (2003).

EXPLORING THE BIOLOGICAL PROTECTIVE ROLE OF CAROTENOIDS BY RAMAN SPECTROSCOPY: MECHANICAL STRESS OF CELLS

F. NEKVAPIL[1,2], CS. MÜLLER MOLNÁR[1,3], S. TOMŠIĆ[4], S. CINTĂ PINZARU[1*]

ABSTRACT. Carotenoids present a group of tetraterpenoid biomolecules which are well known for their physiological benefits through their remarkable radical scavenging activity and reactive oxygen species quenching. However, little is known about role of carotenoids in relieving mechanical stress. Hence, in this study, we exposed sea urchin fertilized eggs to mechanical stress in form of centrifugation and exploited the advantage of Resonance Raman scattering to probe if the carotenoid profile or their distribution would change after application of the stress. Silver nanoparticles were used ro probe the Raman signal of carotenoids near the cell surface and attempt to achieve SERRS conditions (Surface-enhanced Resonance Raman scattering). We have found that carotenoid concentration notably increased on the cell surface after centrifugation, indicating that carotenoids were mobilized in response to mechanical stress.

Keywords: Raman spectroscopy, mechanical stress, sea urchin eggs, carotenoids

INTRODUCTION

Silver nanoparticles (AgNPs) are often used in micro-analytical Raman spectroscopy for detection of SERS (Surface-enhanced Raman scattering) signal from cells and tissues owing to their relatively strong electromagnetic field enhancement

[1] *Biomolecular Physics Department, Babeş-Bolyai University, Str. Kogălniceanu 1, RO 400084 Cluj-Napoca, Romania*

[2] *Physics of Nanostructured Systems Department, National Institute for Development of Isotopic and Molecular Technologies, Str. Donat 67-103, 400293 Cluj-Napoca, Romania*

[3] *Mass Spectrometry, Chromatography and Applied Physics Department, National Institute for Development of Isotopic and Molecular Technologies, Str. Donat 67-103, 400293 Cluj-Napoca, Romania*

[4] *Department of Aquaculture, University of Dubrovnik, Str. Ćira Carića str. 4, 20 000 Dubrovnik, Croatia*

* *Corresponding author: simona.cinta@phys.ubbcluj.ro*

by surface plasmon resonance (SPR), [1-6]. It has been shown previously that distinct Raman and SERS signal of carotenoids can be recorded from live cells and tissue extracts by AgNPs [2-6]. Although chemical protective role of carotenoids is well studied and discussed [7,8], the potential involvement of carotenoids in responses to other kinds of stress, like mechanical insult, is not well investigated yet.

Sea urchins are marine grazing herbivorous invertebrates (Fig. 1). Adult sea urchins are generally resistant to organic and heavy metal pollution [9]. However, the majority of sea urchin species are broadcast spawners, meaning that both the males and the females release their gametes (reproductive cells) freely into sea water [9], where the fertilization and early development takes place. Hence, their early life stages, the gametes, embryos and larvae are directly exposed to environmental chemical and physical factors.

Fig. 1 Photograph of sea urchins in their native environment.

Our previous study has shown that Raman spectroscopy probing of native, mature eggs of the sea urchin *Paracentrotus lividus* induces pre-resonant excitation of carotenoids, whereby the Raman signal represents a mixture of mainly echinenone

and β-carotene [8]. The next developmental step after egg maturation is the fertilization, whereby a rigid protective envelope, composed of proteins and mucopolysaccharides, is raised around the eggs [10,11]. The purpose of the fertilization envelope is, *inter alia*, to protect the developing embryo from the physical environment. In this study, we investigate local changes of carotenoid profile or distribution in the sea urchin *Paracentrotus lividus* eggs after application of mechanical stress, in order to study the involvement of carotenoids in response to this kind of aggression.

EXPERIMENTAL

Obtaining of sea urchin eggs

Sea urchin gametes were obtained by artificial spawning of a male and of three females by injection of KCl solution (1 M). Male seminal fluid was collected "dry", while females were inverted on a beaker to release eggs into filtered natural sea water (filtering with Milipore vacuum filtration system, 0.45 μm pore size). Gametes were subsequently combined and gently stirred to promote fertilization. 5 minutes later, fertilized eggs were sieved through a 50 μm mesh to remove remaining gametes and debris. Optical micrographs of eggs were taken on an Olympus IX71 inverted microscope. More details on the employed spawning method can be found in references 6,8 and 12. Sea urchins were returned to the sea at the site of collection once the gametes have been collected.

Exposing the eggs to mechanical stress

Obtained clean suspension of fertilized eggs was subjected to mechanical stress by centrifuging for 10 minutes at 2000 rpm in a lab centrifuge (50 ml tube capacity), firstly to obtain a concentrated mass of intact eggs, and further to evaluate the possible physiological reaction of centrifuged eggs relative to non-centrifuged ones. In order to localize Raman signal probing to cell surface and eliminate strong carotenoid signalling from egg interior, concentrated egg suspension was drop-coated onto SpectRIM hydrophobic plate, and covered by a droplet of colloidal AgNPs after water evaporation.

Synthesis of AgNPs

The hydroxylamine-reduced colloidal AgNPs were prepared by dissolving of 0.017 g of $AgNO_3$ in 90 ml of distilled water [13]. A second solution was prepared by dissolving of 0.021 g of $NH_2OH \cdot HCl$ in 5 ml of water, and 4.5 ml of 0.1 M sodium hydroxide was further added. The second solution was rapidly added to first, $AgNO_3$ solution, and a grey-brown solution with absorption maximum at 418 nm was obtained in a few seconds.

Raman spectroscopy measurements

Raman spectroscopy measurements of dry sea urchin eggs deposited on a SpectRIM plate by drop-coating method [8] was conducted with a Renishaw InVia Reflex confocal Raman microscope, using the Cobolt DPSS laser emitting at 532 nm. The 20x objective (NA 0.35) was used for viewing the sample and focusing the laser beam. This configuration resulted in the laser spot size of about 1 µm. Spectra were recorded with 0.5 cm^{-1} spectral resolution, in ~100 to 1800 cm^{-1} range. In both Resonance Raman and SERRS measurements, spectra were acquired by a single 1 s exposure under 100 mW laser power.

This study did not require ethical approval. However, all applicable international, national, and/or institutional guidelines for the care and use of experimental animals were followed.

RESULTS AND DISCUSSION

The fertilized eggs were spherical in shape, with the diameter of about 90 µm, and yellowish to orange in colour owing to high content of carotenoids [8] (Fig. 2). The fertilization envelope was observed as a thin layer around the eggs (Fig. 2c). It forms a physical coat around the eggs with about 10 µm of perivitelline space between the envelope and egg cell membrane.

The normal Raman signal of centrifuged fertilized eggs featured only strong pre-resonance carotenoid signal on top of characteristic weak incremental background (Fig. 2a, red spectra), a signal described previously by Nekvapil et al. [8]. This means that the fertilization envelope enables the passage of incident laser beam and the scattered photons. The three main bands were observed here at 1004, 1154 and 1514 cm^{-1}, which in this case indicates a carotenoid mixture of echinenone and β-carotene [8].
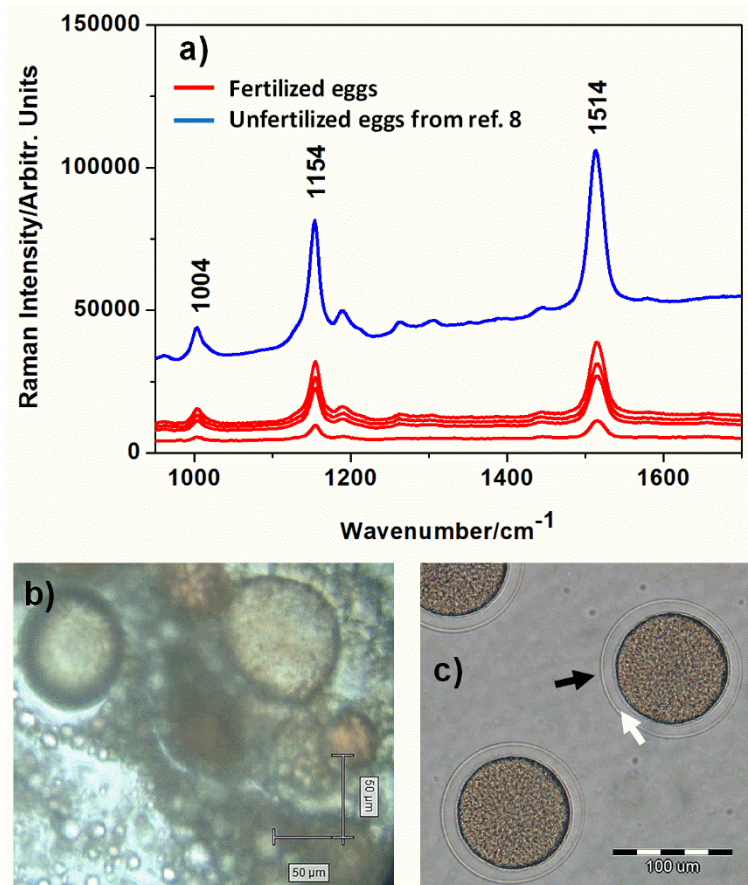
Fig. 2 Analysis of native sea urchin *Paracentrotus lividus* eggs: a) multiple pre-resonance Raman spectra acquired from native fertilized eggs (red), compared to averaged Raman signal of unfertilized eggs from ref. 8 (blue); b) micrograph of unfertilized eggs taken on the Raman microscope; c) micrograph of fertilized eggs taken on inverted brightfield microscope (black arrow - fertilization envelope, white arrow - perivitelline space).

On the contrary, SERRS signal of uncentrifuged fertilized eggs (Fig. 3) were notably complex, presumably reflecting the numerous modes of the envelope material adsorbed onto AgNPs. The modes around 141 and 220 cm^{-1} indicate the aggregation of AgNPs [4]. In between the multitude of bands, SERRS modes at 1079, 1174, 1367, 1510, 1575 and a shoulder at 1649 cm^{-1} could be distinguished, highlighted by red labels in Fig. 3, which are close to SERS modes of β-carotene [5].
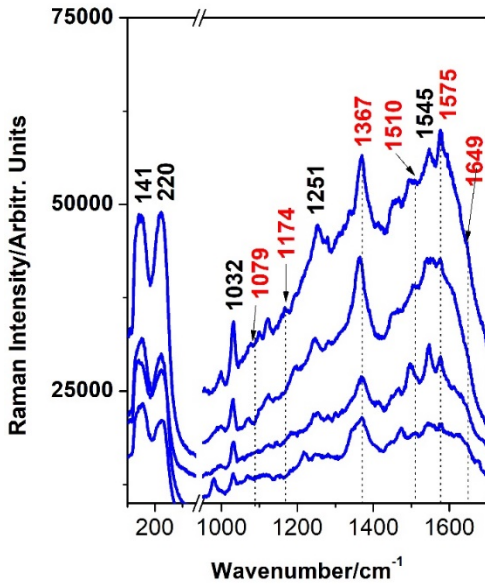
Fig. 3 SERS spectra of native, uncentrifuged fertilized sea urchin *Paracentrotus lividus* eggs, featuring bands of the fertilization envelope material and low-concentration β-carotene bands (labelled in red).

The signal of centrifuged fertilized eggs featured stronger Raman signal of carotenoids (Fig. 4). Acquisition of pre-resonance Raman signal rather than SERRS presumably occurred due to the phenomenon of SERS damping, where only the first molecular layer adsorbed onto AgNPs gives SERS signal, while increase of carotenoid concentration also increases the Resonance Raman signal, which is stronger and
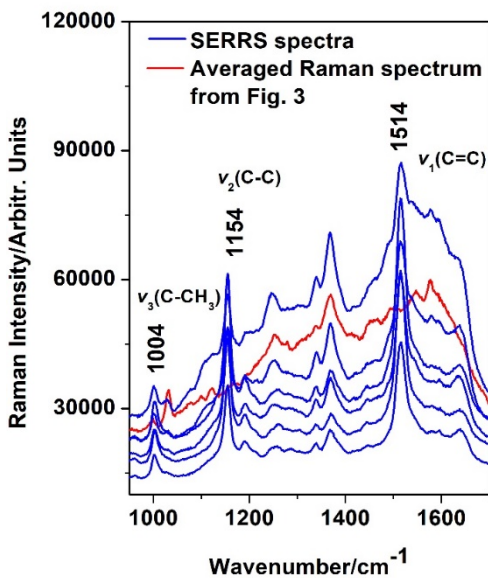
Fig. 4 Multiple SERRS spectra acquired from sea urchin *Paracentrotus lividus* centrifuged fertilized eggs (blue) compared to a representative spectrum of uncentrifuged fertilized eggs. Note the higher intensity of carotenoid bands at 1004, 1154 and 1514 cm^{-1} after centrifugation (blue spectra).

occludes the comparatively weaker SERS signal [5]. The conclusion of this observation is that the carotenoid concentration increased in or very near to the fertilization envelope.

Carotenoids were previously shown to exhibit remarkable free radical scavenging activity [7], hence their role in chemical defence of cells and tissues. In this study, we have shown, by detecting increased concentration of carotenoids near the fertilization envelope, that carotenoids may also have some role to play in mechanical stress relieving. A previous study that employed centrifugation of sea urchin oocytes has shown that centrifugation temporarily changes the spatial distribution of cell organelles, and that normal organization of the cell interior is restored later [14]. Hence, centrifugation could not have permanently narrowed the perivitelline space and so brought the cell itself closer to the envelope, where AgNPs are aggregated. It is possible that mechanical stress induces chemical insults within the cell, and that is where carotenoids may come into play to remediate oxidative stress.

The localization of SERS signal from the fertilization envelope is supported by the fact that the signal of only low-concentration β-carotene signal along with general indicator bands of proteins [15] was recorded, rather than strong carotenoid signal which would be recorded under Resonance Raman excitation only. The conclusion on increased concentration of carotenoids near the fertilization envelope is supported by the fact that electromagnetic enhancement of atomic vibrations by SPR extends only a few nanometres from the nanoparticles surface, which is much smaller that the width of perivitelline space. Thus, the phenomenon of SERS damping by carotenoids must have occurred near the fertilization envelope.

Detection of increased carotenoid content near the fertilization envelope after the mechanical stress, i.e. centrifugation, raises a new question that has to be investigated by other methods: a physiological mechanism must exist, which rapidly transports carotenoids, which are lipid-soluble, from cells into the envelope, which is not believed to be rich in lipides. Hence the question of means of cellular transport of carotenoids through media where they are not soluble.

CONCLUSION

In this paper we have shown, using Resonance Raman scattering and Surface-enhanced Raman scattering, that mechanical stress to sea urchin eggs, in form of centrifugation within non-lethal parameters, induces a shift in cellular carotenoids distribution. The carotenoids are engaged presumably because centrifugation induces oxidative stress to the eggs.

ACKNOWLEDGEMENTS

REFERENCES

1. S. Cintă Pinzaru, Cs. Müller, I. Ujević, M. M. Venter, V. Chiş, B. Glamuzina, *Talanta*, 187, 47 (2018).
2. S. Cintă Pinzaru, M. Ardeleanu, I. Brezeştean, F. Nekvapil, M. M. Venter. *Anal. Methods-UK,* 11, 800 (2019).
3. F. Nekvapil, S. Tomšić, S. Cintă Pinzaru, "Book of abstracts of the International conference Air and water components of the environment", University Press, Cluj-Napoca, 2018, page 27.
4. S. Cintă Pinzaru, Cs. Müller, S. Tomšić, M. M. Venter, I. Brezeştean, S. Ljubimir, B. Glamuzina, *RSC Adv.,* 6, 42899 (2016).
5. S. Cintă Pinzaru, Cs. Müller, S. Tomšić, M. M. Venter, B. I. Cozar, B. Glamuzina, *J. Raman Spectrosc.,* 46, 597 (2015).
6. F. Nekvapil, "Master thesis: Određivanje sadržaja karotenoida hridinskog ježinca, Paracentrotus lividus uz pomoć Raman spektroskopije", University of Dubrovnik, 2017. URL: https://repozitorij.unidu.hr/islandora/object/unidu:280 (Accessed 8. Nov 2019)
7. M. Tsuchiya, G. Scita, H-J. Freisleben, V. E. Kagan, L. Packer, *Methods Enzymol.,* 213, 440 (1992).
8. F. Nekvapil, I. Brezeştean, S. Tomšić, Cs. Müller, V. Chiş, S. Cintă Pinzaru, *Photochem. Photobiol. Sci.,* 18, 1933 (2019).
9. C. E. Boudouresque, M. Verlaque. Sea urchins: biology and ecology, 3rd edition. *Dev. Aquacult. Fish. Sci.*, 38, 297 (2013).
10. G. Chizak, R. Peter, "The sea urchin embryo: biochemistry and morphogenesis", Springer-Verlag Berlin, Heidelberg, New York, 1975, chapter 3.
11. G. S. Kopf, G. W. Moy, V. D. Vacquier, J. *Cell. Biol*., 95, 924 (1982).
12. M. Tsushima, T. Kawakami, M. Mine, T. Matsuno, *Invertebr. Reprod. Dev.,* 32, 149 (1997).
13. N. Leopold, B. Lendl, *J. Phys. Chem. B,* 107(24), 5723 (2003).
14. J. M. Brooks, G. M. Wessel, *Develop. Biol.,* 261, 353 (2003).
15. A. Rygula, K. Majzner, K. M. Marzec, A. Kaczor, M. Pilarczyk, M. Baranska, *J. Raman Spectrosc.,* 44, 1061 (2013).

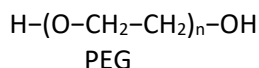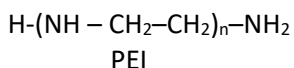# SOME ASPECTS OF THERMODYNAMIC PROPERTIES OF ETHYLENIMINE AND ETHYLENE GLYCOL LINEAR POLYMERS

R. D. PAŞCA[1,2*], T. A. BEU[1*]

ABSTRACT The two biopolymers, namely polyethy-lenimine (PEI) and polyethylene glycol (PEG) in linear configurations, with a different range of polymerization, containing between 3 and 25 repeat units, have been studied by means of 3 functions of state: enthalpy, entropy and Gibbs free energy in standard conditions, using density functional (DFT) calculations. The preliminary data show that the stability of the two polymers decreases with the increasing of their degree of polymerization, namely with the increasing of their chain length.

Key words: Thermodynamics, functions of state, biopolymers, PEI, PEG.

INTRODUCTION

Polyethylenimine (PEI) or polyaziridine and polyethylene glycol (PEG) also known as polyethylene oxide (PEO) are two polymers with a similar structure:

$$\text{H-(NH} - \text{CH}_2 - \text{CH}_2)_n - \text{NH}_2 \qquad \text{H} - (\text{O} - \text{CH}_2 - \text{CH}_2)_n - \text{OH}$$
$$\text{PEI} \qquad\qquad\qquad \text{PEG}$$

Both contain ethylene groups -CH_2CH_2-, separating the ether (-O-), respectively secondary amine (-NH-) groups. Both can exist in linear forms, as presented in the formulas above or branched forms. PEI can also present dendrimeric forms [1], while for PEG there are also starPEGs and combPEGs. For the beginning, here only

[1] *Department of Biomolecular Physics, Faculty of Physics, Babeş-Bolyai University, Cluj-Napoca, M. Kogalniceanu str., no1, 400028, Romania*

[2] *Department of Molecular and Biomolecular Physics, National Institute for Research and Development of Isotopic and Molecular Technologies, Donath str., no 67-103, Cluj-Napoca, 400293, Romania*

* *Corresponding authors: roxana.pasca@ubbcluj.ro, titus.beu@phys.ubbcluj.ro*

the linear forms will be considered. The name PEG is used mainly for oligomers and polymers with low degrees of polymerization, n (e.g. under 400-500) [2], while PEO is referred for higher degrees of polymerization which can attend some hundreds of thousands (molar weight as high as 10^7g/mol). Likewise, PEI of various polymerization degrees, from oligomers to polymers with molar weight of about 10^6 is used [3]. The basic amine groups in PEI can be easily protonated, conferring a polycationic character to the polymer [4, 5].

Both polymers have multiple utilizations [6]. PEGs have biological and medical applications, e.g. as encapsulating agents for drug delivery [7], for coating gene therapy vectors against inactivation by the immune system [8].

PEI is also a multipurpose polymer used in adhesives, cosmetics, detergents, in the cellulose and paper industry [9, 10]. Much attention is paid to its use as carbon dioxide absorbent [11]. In biology, it is used as transfection agent for DNA [12]

For crystallized PEG oligomers (up to n= 48) secondary helical structures were observed [2]. For polymers above the glass transition temperature and in solution, the polymer theory predicts a random coil configuration. The molecular configurations of PEG (n= 27) and PEO were simulated and analyzed in water solution [13] using Charmm c33b2 program [14]. For liquid PEG molecular dynamics simulations were performed using various force fields [15], and with the OPLS-AA force field its hydrogen-bond structure was discussed [16]. All atom molecular dynamics simulation was also used to study the role of PEG in drug delivery [17]. Calculations of this type were also applied for the study of intercalated in clay [18]. Some thermodynamic properties for liquid PEG were studied from its volume [19].

PEI was as well studied theoretically, especially for its action as a proton acceptor, a real "proton sponge" in acidic medium [20]. For linear chains of PEI in solution, molecular dynamic simulations [20] showed that in basic medium (high pH) the chain presents a coil configuration, while in strong acidic conditions (low pH) the chains are elongated. The thermodynamics of CO_2 adsorption on PEI was also investigated [21]. Molecular dynamics and Monte Carlo simulations were used to study the protonation behavior of PEI in solution [22], and the modelling of CO_2 adsorption on PEI was achieved [23].

Some quantum chemical calculations for PEI and PEG were also realized. The mechanism for the electrochemical polymerization of diethylenetriamine (the dimer, n = 2 in the series of PEI) to linear PEI was studied by ab initio quantum chemical calculations at the Hartree–Fock level with Gaussian 98W of standard reaction free enthalpies, finding that the formation of linear PEI is more probable as that of branched PEI [24]. A similar investigation was made for the electrochemical polymerization mechanism of p-phenylenediamine [25]. The monomer of PEI, EDA

(ethylenediamine, n = 1) was studied along with different other aliphatic diamines by ab initio (at Hartree-Fock level) and density functional calculations, giving an insight on the thermodynamics of their protonation [26]. For linear PEI and linear polypropylenimine (n = 1…5), ab initio and quantum-mechanical calculations at diverse levels were compared by computing their vibrational frequencies and intensities after geometry optimization [27].

For PEG (n = 1-5, 10, 20, 30), quantum chemical calculations using DFT, ab initio Hartree-Fock and semiempirical PM3 were used to calculate HMO and LUMO energies and quantities related to these, and adsorption energy on Al surface were evaluated, for correlations with the inhibitor effect of these compounds on the corrosion of Al [28]. The vibrational spectrum of polyethylene was compared with the spectrum of PEG, obtained using Gaussian [29]. The influence of intramolecular hydrogen bonds in PEG (n = 2-5) was studied by DFT calculations and MD simulations [30]. Quantum chemical calculations for PEG (n = 1-5) were also used to calculate saturation vapor pressures, after selecting the lowest energy conformers [31].

Here we test the capacity of quantum chemical computation to characterize the stability of polymeric molecules by calculation of thermodynamic quantities.

THEORETICAL DETAILS

Fully extended PEI and PEG molecules with different degrees of polymerization were used as initial configurations for our investigations, using the Gaussian 09W package [32] at the DFT PBEPBE 6-311G (d,p) level of theory. The studied molecules have been built using Gauss View 5.0. Thermodynamic quantities at standard temperature (298 K) have been calculated using the thermochemistry output from Gaussian, as obtained in the program by using the equations of Statistical Thermodynamics. These calculations were made for all the terms of the two polymer homologous series, from n = 3 to 20.

RESULTS AND DISCUSSION

The structures of the linear polymers with different degrees of polymerization, n, are presented in Fig. 1 for PEI, with n = 5 …15 mers (structure units) and Fig. 2 for PEG, with n = 5…15 mers.

Some of the calculated Gibbs free energy (G) values expressed in kcal/mol and enthropy (S) values in cal/(mol.K) units for different PEI molecules [n = 5…15] are given in Table 1 and the similar quantities for PEG [n = 5…15] in Table 2. They were

obtained by reporting the thermodynamic quantities given by the DFT calculations to the number of mers, n. They are therefore average molar quantities, per mole of unit of structure (mer). Of course, the thermodynamic values for the different mers are not the same along the polymer chain. In particular, the two terminal mers differ from the inner ones by a hydrogen atom and thus have lower energies, but their effect on the total energies decreases with increasing n values

The Gibbs free energy was calculated because it is a measure of the thermodynamic stability of the molecules. The lower the value of this quantity, the more stable the compound. The negative values suggest a thermodynamic stability. The values are lower for the PEG molecules as compared with the corresponding PEI molecules, due to the presence in the former of the more electronegative oxygen atoms, replacing the NH groups of PEI.

The entropy values are small, as expected given the restriction imposed on the configurations of the molecules: fully extended configurations as found in solid state. They are the same for the two series of molecules, in the limits of the used model
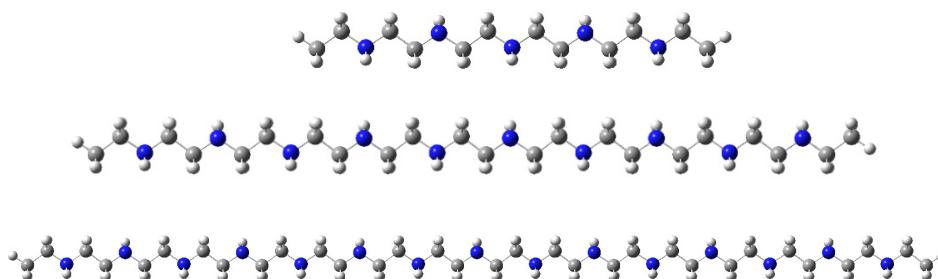
Fig. 1. PEI containing 5, 10 and 15 mers. Gray circles represents the carbon atoms, blue circles the nitrogen atoms, and the smaller circles – the hydrogen atoms

In Fig. 3, the values of the molar Gibbs free energy in kcal/mol are represented against the number of mers for PEI (n from 3 to 20) and in Fig. 4 for PEG (n from 3 to 20). From both figures 3 and 4, an analogous increase of the Gibbs free energy per mole of mers with the degree of polymerization, n, is observed. That means a slightly decreasing stability for the higher polymers. It is a logarithmic variation, faster for the lower terms of the polymer homologous series but slowing down for the higher terms, where the stability becomes practically constant up from 15-20 mers.
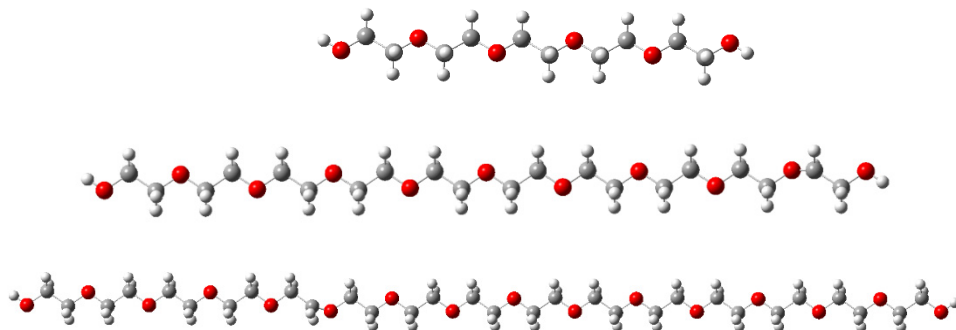
Fig. 2. PEG containing 5, 10, and 15 mers, Gray circles represents the carbon atoms, red circles the oxygen atoms, and the smaller circles – the hydrogen atoms

Table 1. Some G and H values in kcal/mol and S values
in cal/molK for PEI

Molecule	G, kcal/mol	H, kcal/mol	S, kcal/mol
PEI5	-150	-143	24
PEI10	-142	-137	18
PEI15	-139	-135	15
PEI20	-138	-134	14

Table 2. Some G and H values in kcal/mol and S values
in cal/molK for PEG

Molecule	G, kcal/mol	H, kcal/mol	S, kcal/mol
PEG5	-169	-163	19
PEG10	-161	-157	13
PEG15	-158	-155	11
PEG20	-157	-154	10
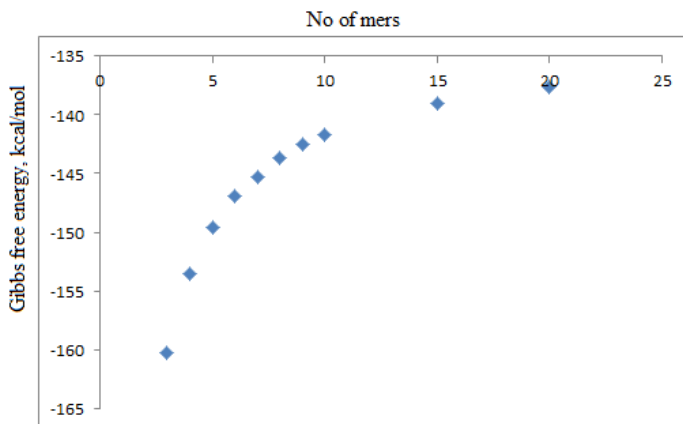
Fig. 3. G in kcal/mol against number of mers for PEI
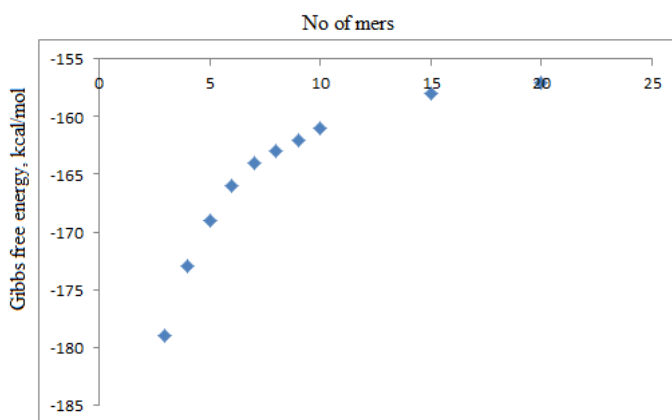
Fig. 4. G in kcal/mol against number of mers for PEG

These results were obtained using fully extended configurations of the polymer molecules. However, the flexibility of the carbon backbone of the molecular chains leads to the random coil conformation of polymers with higher degree of polymerization, in fluid state or in solution. This would increase the entropy of the higher polymers and, in consequence, decrease their free energy, thus showing a higher thermodynamic stability.

Taking into account the intramolecular hydrogen bonds in PEG [30] would also affect the configuration of the molecules, but only for the lowest values of n, since in higher polymers the contribution of free −OH groups becomes negligible.

CONCLUSIONS

Thermodynamic characteristics of PEI and PEG polymers of different degrees of polymerization (up to 20), as estimated from a computational chemistry model, suggest a slight decrease of stability for the first terms of the two polymer homologous series. A more elaborate model, taking into account the flexibility of macromolecule segments for higher degrees of polymerization, should complete these preliminary results.

ACKNOWLEDGEMENT

REFERENCES

1. O. Yemul, T. Imae, *Colloid Polym. Sci.*, 286, 747 (2008).
2. A.C. French, A.L. Thompson, B.G. Davis, *Angew. Chem. Int. Ed.*, 48, 1248 (2009).
3. L. Avadiar, Y. K. Leong, A. Fourie, *Powder Technol.,* 254, 364 (2014).
4. T. A. Beu, A. E. Ailenei, A. Farcaş, *J. Comput. Chem.,* 39, 2564 (2018).
5. T. A. Beu, A. Farcaş, *J. Comput. Chem.,* 38, 2335 (2017).
6. J. M. Harris (editor), „Poly (ethylene glycol) Chemistry. Biotechnical and Biomedical Applications", Plenum Publ.Co., New York, 1992.
7. J. M. Harris, R. B. Chess, *Nat. Rev. Drug Discov*., 2, 214 (2003).
8. F. Kreppel, S. Kochanek, *Mol. Ther.,* 16, 16 (2007).
9. Z. Chen, M. Deng, Y. Chen, G. He, M. Wu, J. Wang, *J. Membr. Sci.*, 235, 73, (2004).
10. L. Wagberg, *Nord. Pulp Paper Res. J.,* 15, 586 (2000).
11. S. Satyapal, T. Filburn, J. Trela, J. Strange, *Energy Fuels*, 15, 250 (2001).
12. A. Akinc, M. Thomas, A.M. Klibanov, R. Langer, *J. Gene Med.*, 7, 657 (2004).
13. H. Lee, R. M. Venable, A. D. MacKerrel Jr., R. W. Pastor, *Biophys. J.*, 95, 1590 (2008).
14. B. R. Brooks, R. E. Bruccoleri, B. D. Olafson, D. J. States, S. Swaminathan, M. Karplus, *J. Comput. Chem.,* 4, 187 (1983).
15. L. Saiz, J. A. Padro, E. Guardia, *J. Chem. Phys.,* 114, 3187 (2001).
16. A. Kaiser, O. Ismailova, A. Koskela, S. E. Huber, M. Ritter, B. Cosenza, W. Benger, R. Nazmutdinov, M. l. Probst, *J. Mol. Liq.,* 189, 2 (2014).
17. A. Bunker, *Phys. Procedia*, 34, 24 (2012).
18. R. W. A. Franco, C. A. Brasil, G. L. Mantovani, E. R. de Azevedo, T. J. Bonagamba, *Materials*, 6*,* 47, (2013).
19. F. M. Sannaningannavar, S. N. Patil, B. S. Navati, R. M. Melavanki, N. H. Ayachit, *Polym. Bull.*, 70, 3171 (2013).

20. C. Kumar Choudhury, S. Roy, *Soft Matter*, 9, 2269 (2013).
21. M. J. Al-Marri, K. Al-Saad, M. A. Saad, D. J. Cortes, M. M. Khader, *J. Phys. Chem. Biophys.*, 7, 1 (2017).
22. J. D. Ziebarth, Y. M. Wang, *Biomacromolecules*, 11, 29 (2010).
23. X. Shen, H. Du, R. H. Mullins, R. R. Kommalapati, *Energy Technol*., 5, 822 (2017).
24. B. Lakard, G. Herlem, B. Fahys B., *J. Mol. Struct. (Theochem)*, *593(1-3),* 133 (2002).
25. B. Lakard, G. Herlem, S. Lakard, B. Fahys, *J. Mol. Struct. (Theochem)*, *638*, 177 (2003).
26. B. Lakard, G. Herlem, M. Herlem, A. Etcheberry, J. Morvan, B. Fahys, *Surf. Sci., 502-503*, 296 (2002).
27. S. Lakard, G. Herlem, B. Lakard, B. Fahys, *J. Mol. Struct. (Theochem)*, *685*, 83 (2004).
28. M.K. Awad, *Can. J. Chem.*, *91(4)*, 283 (2013).
29. E. Talebian, M. Talebian, *Optik, 125(1)*, 228 (2014).
30. M. Kozlowska, J. Goclon, P. Rodziewicz, *ChemPhysChem, 17(8)*, 1143 (2016).
31. U. K. Krieger, F. Siegrist, C. Marcolli, E. U. Emanuelsson, F. M. Gbel, M. Bilde, A. Marsh, J. P. Reid, A. J. Huisman, I. Riipinen, N. Hyttinen, N. Myllys,T. Kurten, T. Bannan, C. J. Percival, D. Topping, *Atmos. Meas.Tech.*, *11*, 49 (2018).
32. Gaussian 09, Revision A.02, M. J. Frisch, G. W. Trucks, H. B. Schlegel, G. E. Scuseria, M. A. Robb, J. R. Cheeseman, G. Scalmani, V. Barone, B. Mennucci, G. A. Petersson, H. Nakatsuji, M. Caricato, X. Li, H. P. Hratchian, A. F. Izmaylov, J. Bloino, G. Zheng, J. L. Sonnenberg, M. Hada, M. Ehara, K. Toyota, R. Fukuda, J. Hasegawa, M. Ishida, T. Nakajima, Y. Honda, O. Kitao, H. Nakai, T. Vreven, J. A. Montgomery, Jr., J. E. Peralta, F. Ogliaro, M. Bearpark, J. J. Heyd, E. Brothers, K. N. Kudin, V. N. Staroverov, R. Kobayashi, J. Normand, K. Raghavachari, A. Rendell, J. C. Burant, S. S. Iyengar, J. Tomasi, M. Cossi, N. Rega, J. M. Millam, M. Klene, J. E. Knox, J. B. Cross, V. Bakken, C. Adamo, J. Jaramillo, R. Gomperts, R. E. Stratmann, O. Yazyev, A. J. Austin, R. Cammi, C. Pomelli, J. W. Ochterski, R. L. Martin, K. Morokuma, V. G. Zakrzewski, G. A. Voth, P. Salvador, J. J. Dannenberg, S. Dapprich, A. D. Daniels, O. Farkas, J. B. Foresman, J. V. Ortiz, J. Cioslowski, and D. J. Fox, Gaussian, Inc., Wallingford CT, 2009.

FEEDBACK CONTROL OF DC MOTORS WITH LONG RANGE HC 12 TRANSCEIVER AND ARDUINO

M. TODICA[1*]

ABSTRACT. The work demonstrates the possibility to control DC motors at long distance with feedback. The system uses the radio transceivers HC 12, Arduino board and LCD keypad shield. Complete description of the hardware and software parts of the system is presented.

Keywords: DC feedback control, HC12 transceiver, Arduino.

INTRODUCTION

One of the problems occurring on remote control devices at long distance is the confirmation of the achievement of the command, on the other word the feedback the action, [1]. For this purpose the actuator must have the capability to send back to the sender the confirmation of the achievement of the order. That supposes a bilateral communication between the sender and the receiver, [12]. In the radio transmission this task can be done using transceivers. Bluetooth devices are actually very popular modules fulfilling this task, being included frequently in phones, computers, TV, etc. The range of such devices is of the order of few meters and the feedback is not necessarily because the user can perceive with its own senses the achievement of the command. The situation is different when using long range devices, as HC 12 Bluetooth modules, which can send data over hundred of meters, [2]. In this case the feedback is absolutely necessarily.

This work proposes a simple and cheap solution to provide a feedback between the sender and receiver using the Arduino platform, [3]. As examples the project was used to control two low power DC motors.

---

[1] *"Babes-Bolyai" University, Faculty of Physics, M. Kogalniceanu No 1, 400084 Cluj-Napoca, Romania*
* *Corresponding author: mihai.todica@phys.ubbcluj.ro*

EXPERIMENTAL

For this project we need two Arduino Uno boards, two HC12 Bluetooth modules, two 3-6 V DC motors, one MX 1805 H bridge and one LCD 1602 keypad shield Arduino compatible. The system consists of two parts, the sender and the receiver.
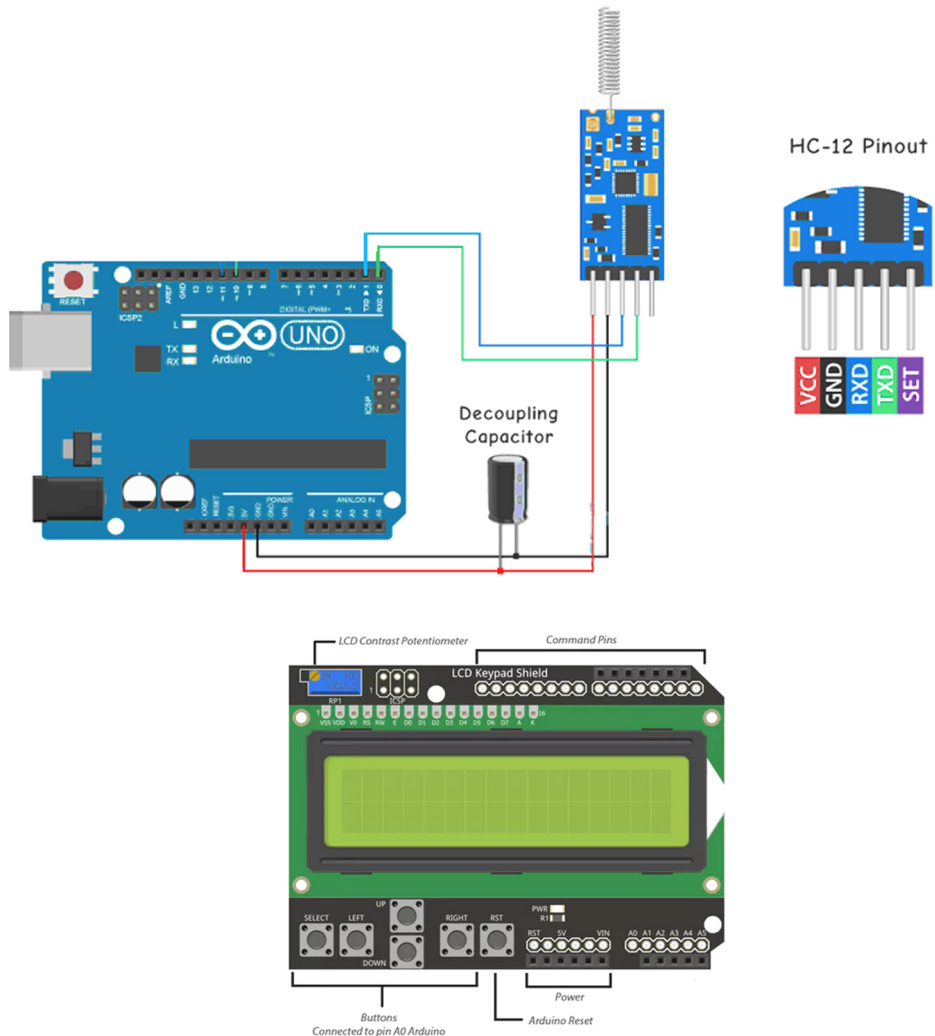
Fig. 1. The sender with HC12 module and Arduino Uno.
The image of the LCD keypad shield.

The sender is very simple. The LCD keypad is plugged onto the Arduino board and then the HC 12 is soldered on the back side of the Arduino board, as shown in figure 1. The correspondence of the pins is shown in table 1.

Table 1

HC12	Arduino
Vcc	+5V
GND	GND
Tx	Rx
Rx	Tx
Set	NC

It is suitable to connect a decoupling capacitor of 100 F on the power rails of HC12 to prevent fluctuations of the alimentation voltage.

The receiver contains one Arduino Uno board to which the HC 12 is attached in the same manner as for the sender, (Fig. 2). On the pins D12-D14 are connected the entries IN1-IN4 of the H bridge. The GND of the H bridge is connected
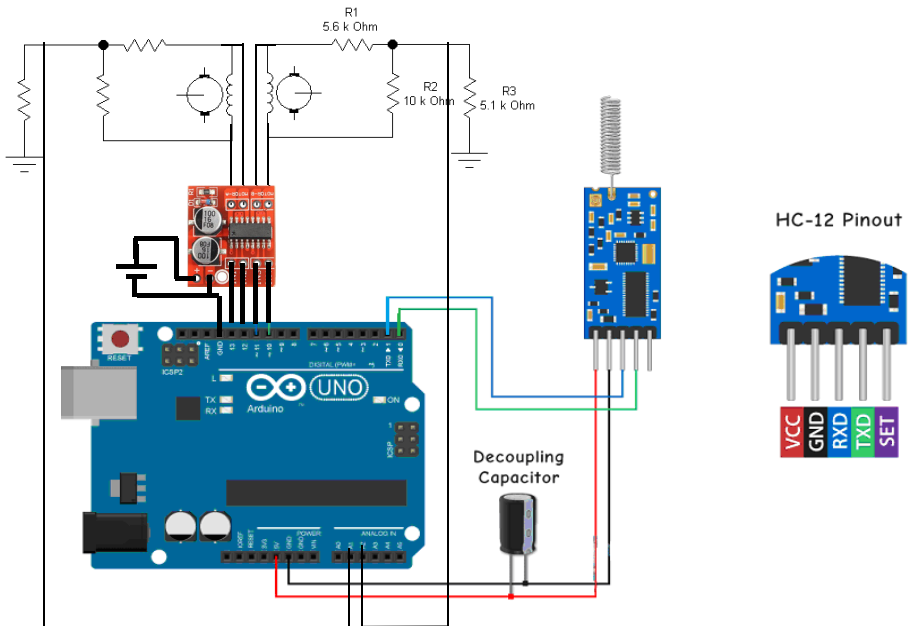

Fig. 2. The receiver

to the GND of Arduino board, and the +V is connected to a separately battery power, as shown in figure 2. The DC motors are connected to the outputs of the H bridge. The voltage applied to the motor is collected by a resistive divider and applied to the entries A1 and A2 of the Arduino board for the feedback, [4, 5, 11].

RESULTS AND DISCUSSION

The important piece of this system is the HC 12 Bluetooth transceiver. It is a wireless serial port communication module working in the frequency band from 433.4 MHz to 473.0 MHz. The domain is divided into 100 channels separated by 400 KHz each to other. The transmission power can be set in the range -1dBm (0.79mW) to 20dBm (100mW), and the receiving sensitivity can be set in the range -117dBm (0.019pW) to -100dBm (10pW). These values, as well as the working frequency, can be set accessing the AT command of the module, [2]. However we can use the modules as they come from the manufacturer, without any supplementary setting, because they are set to work at the maximum power and high reception sensitivity on the cannel 001. The system contains two HC 12 modules set as sender and receiver.
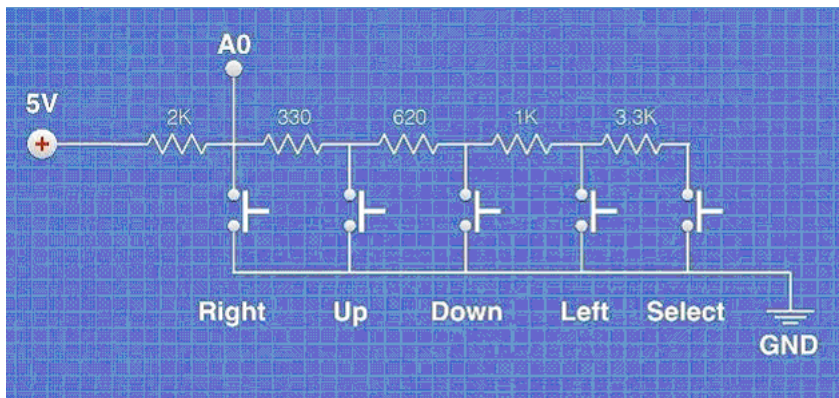
Fig. 3. The inner voltage resistive divider of the LCD keypad shield

The sender sends analog data read from a resistive voltage divider, included into the LCD keypad shield. The analog values are applied to the pin A0 which is connected to the inner resistive divider as shown in figure 3. When pressing one of the buttons Right, Left, Up, Down, Select, a given value of the voltage, between 0

and 5V, is applied to the pin A0. The ADC of Arduino converts these analog values in binary data from 0 to 1023. In the Arduino code of the sender we divide by 4 these data. This conversion is necessarily because the data from 0 to 255 can be sent over the Bluetooth device as 1 byte, which is easier to be accepted on the receiver side, [6, 7]. The module HC12 is set on sender mode by the code.

The code for the sender.

```
#include <LiquidCrystal.h>
LiquidCrystal lcd(8, 9, 4, 5, 6, 7);
int x;
int M1=0;
int M2=0;

void setup() {
Serial.begin(9600); // Default communication rate of the Bluetooth module
lcd.begin(16, 2);
}

void loop() {
 x = analogRead(A0);
 //read analog data for LCD Keypad
 Serial.write(x/4); // Dividing by 4 for converting from 0 - 1023 to 0 - 256, (1 byte) range
 // Send the values via the serial port to the slave HC-05 Bluetooth device
 delay(20);

 lcd.setCursor(0, 0);
    lcd.print("sent x=");
    lcd.print(x/4);
 lcd.print("       ");
 delay(20);
//displays locally the sending x data

while (Serial.available() == 0) {}
 M1 = Serial.read();
 //delay(10);
 //Serial.write(val);
```

```
lcd.setCursor(0, 1);
   lcd.print("M1=");
   lcd.print(M1);
   lcd.print("     ");
//displays the value M1 sent back by the receiver for feedback
 M2= Serial.read();
   lcd.setCursor(10, 1);
   lcd.print("M2=");
   lcd.print(M2);
   lcd.print("  ");
//displays the value M2 sent back by the receiver for feedback
}
```

The receiver select the data sent by the sender and command a corresponding DC motor, forward, backward or stop, in function of the values of analog data. The interesting part of the project is the feedback action. The principle of working can be easily understood following the figure 4, which presents a generic H bridge powered by a single voltage battery, with a DC motor connected on its output, [8]. A resistive voltage divider R1/R2 is connected at the ends of the DC motor.
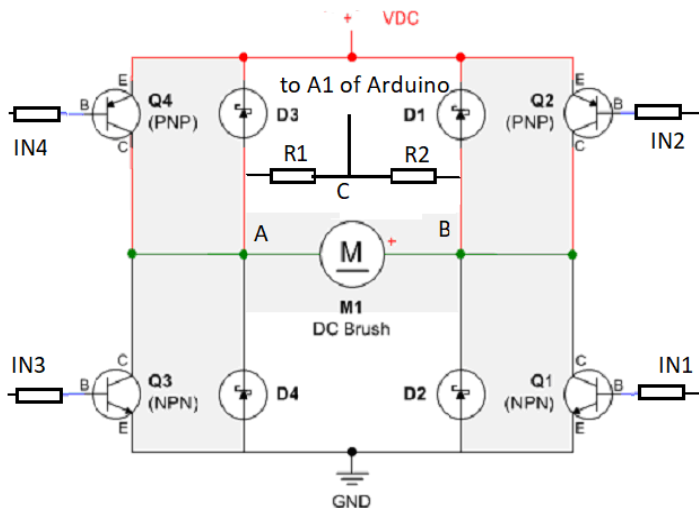
Fig. 4. The generic schema of H bridge.

When the transistors Q1 and Q4 are in ON state, the point A is connected to +Vdc and the B point to the ground. The DC motor will rotate in one direction.

The voltage of the point C of the R1/R2 divider is $V_{C1} = V_{dc} \dfrac{R_1}{R_1 + R_2}$, [9, 10].

When the transistors Q3 and Q2 are in the ON state, the point A is connected to GND and the B point to +Vdc. The DC motor will rotate in opposite direction. The

voltage of the point C of the R1/R2 divider is $V_{C2} = V_{dc} \dfrac{R_2}{R_1 + R_2}$. In both cases

the potential of the point C is positive by rapport to GND and proportional to R1 or R2 in function of which transistors are in ON state. It results the possibility to correlate the rotation direction of the motor to the Vc voltage. This voltage is applied to the entries A1 and A2 of the Arduino. These entries are connected to the ground trough the resistor R3, (Fig. 3). Due to this resistor the real voltage of the

entries A1 and A2 is: $V_{C1} = V_{dc} \dfrac{R_1 R_3}{R_1 R_2 + R_1 R_3 + R_2 R_3}$ and

$V_{C2} = V_{d}c \dfrac{R_2 R_3}{R_1 R_2 + R_1 R_3 + R_2 R_3}$. If the H bridge is not activated the potential

on the entries A1 and A2 is zero, due to the resistor R3. The values of Vc are sending back and displayed on the LCD of the sender. So the feedback is achieved. To do this, the HC 12 module is put on the sender mode for few milliseconds, after that it comes back on the receiver mode. This operation is commanded by the code.

If the values of R1 and R2 are different, the Vc1 and Vc2 voltages are different for the forward and backward rotation of the DC motor. In this manner it is possible to know if the DC motor is rotating and what is the direction of rotation.

The receiver code

```
#define in1 10
#define in2 11
#define in3 12
#define in4 13

int xAxis;
int  x = 0;
int M1=0;//feedback for Motor 1
int M2=0;//feedback for Motor 2
```

```
void setup() {

  pinMode(in1, OUTPUT);
  pinMode(in2, OUTPUT);
  pinMode(in3, OUTPUT);
  pinMode(in4, OUTPUT);

  digitalWrite(in1, LOW);
  digitalWrite(in2, LOW);
  digitalWrite(in3, LOW);
  digitalWrite(in4,LOW);

  Serial.begin(9600);
  // Default communication rate of the Bluetooth module
}

void loop() {

  // Read the incoming data from the
  while (Serial.available() == 0) {}
  x = Serial.read();
  delay(10);

  // Convert back the 0 - 255 range to 0 - 1023, suitable for motor control
  xAxis = x * 4;

  if (xAxis > 50 & xAxis < 170) {
   //forward
   digitalWrite(in1,HIGH);
   digitalWrite(in2,LOW);
   digitalWrite(in3, LOW);
   digitalWrite(in4, HIGH);
   }
 else if (xAxis > 210 & xAxis < 370) {
   //backward
   digitalWrite(in1,LOW);
   digitalWrite(in2, HIGH);
   digitalWrite(in3, HIGH);
   digitalWrite(in4, LOW);
 }
```

```
 else if (xAxis > 400 & xAxis < 650 ) {
   //left
  digitalWrite(in1,LOW);
  digitalWrite(in2, LOW);
  digitalWrite(in3, LOW);
  digitalWrite(in4,HIGH);
 }

 else if (xAxis < 20 ) {
   //right
  digitalWrite(in1,HIGH);
  digitalWrite(in2, LOW);
  digitalWrite(in3, LOW);
  digitalWrite(in4,LOW);
 }
else if (xAxis > 700) {
   //stop
  digitalWrite(in1,LOW);
  digitalWrite(in2, LOW);
  digitalWrite(in3, LOW);
  digitalWrite(in4,LOW);
 }

 M1 = analogRead(A1);
 Serial.write(M1/4);
 //send back data to the sender
 Serial.write("");
  //compulsory for separating M1 and M2 data
    delay(10);

 M2 = analogRead(A2);
 Serial.write(M2/4);

 delay(20);
 }
```

CONCLUSION

The possibility to control two DC motors at long distance with feedback was tested with HC 12 transceiver. These modules are driven by two Arduino UNO boards. Economic and elegant solution for the sender is the use of the LCD keypad Arduino compatible shield. The feedback action was performed collecting the voltage on the ends of the DC motor trough a resistive voltage divider and sending back to the sender. This task is performed using adequate codes for sender and receiver.

REFERENCES

1. M. Todica, *Servo and RGB led feedback with smartphone and Blynk* Research Gate DOI: 10.13140/RG.2.2.23512.08960
2. Dejan Nedelkovski, *Arduino Long Range Wireless Communication using HC-12*, www.HowToMechatronics.com
3. Arduino Website (www.arduino.cc/en/Guide/ Introduction)
4. A Tunyagi, K Kandrai, Z Fülöp, Z Kapusi and A Simon, Phys. Educ. 53 (2018) 035028 (9pp)
5. M. Todica, C. V. Pop, Fizica generala aplicata, Presa Universitara Clujeana, Cluj-Napoca, 2007, ISBN (10)973-610-498-2; ISBN (13) 978-973-610-498-5
6. I. Burda, Microprocesoare si microcontrolere, Presa Universitară Clujeană, Cluj-Napoca, 2002, ISBN 973-610-046-4.
7. D. Rădoiu, G.D. Popescu, Introducere în ştiinţa sistemelor de calcul, Editura Universităţii "Petru Maior", Târgu-Mureş, 1999, ISBN 973-98726-7-0
8. T. A. Antal, Acta Technica Napocensis, Series: Applied Mathematics, Mechanics, and Engineering, Vol. 60, Issue I, March, (2017).
9. R. M. Eisberg, L. S. Lerner, Physics Foundations and Applications, McGraw-Hill, London, 1982, ISBN 0-07-066268-1.
10. B. M. Yavorsky and A. A. Pinsky, Fundamental of Physics, Mir Publishers, Moscow, 1987.
11. S. D. Anghel, Bazele Electronicii analogice si digitale, Presa Universitară Clujeană, Cluj-Napoca, 2007, ISBN: 978-973-610-554-8
12. M. Todica, *Software feedback with HC 12 transceivers and Arduino* Research Gate DOI: 10.13140/RG.2.2.24560.61444